2011

TURBULENCE ACCUMULATION AND AVERAGE IN THE SYMMETRICALLY AND ASYMMETRICALLY STENOSED CAROTID BIFURCATION

Janet Lianne Powell

TURBULENCE ACCUMULATION AND AVERAGE IN THE SYMMETRICALLY AND ASYMMETRICALLY STENOSED CAROTID BIFURCATION

(Spine title: Turbulence in Symmetric and Asymmetric Carotid Bifurcations)

(Thesis format: Integrated-Article)

by

Janet L. Powell

Graduate Program in Physics

A thesis submitted in partial fulfillment
of the requirements for the degree of
Master of Science

The School of Graduate and Post Doctoral Studies
The University of Western Ontario
London, Ontario, Canada

The University of Western Ontario
School of Graduate and Postdoctoral Studies

Certificate of Examination

Supervisor	Examiners
Dr. Tamie Poepping	Dr. Blaine Chronik
Supervisory Committee	Dr. John de Bruyn
Dr. Jeff Hutter	Dr. Chris Ellis
Dr. Eugene Wong	

The thesis by

Janet Lianne Powell

entitled:

Turbulence Accumulation and Average in the Symmetrically and Asymmetrically Stenosed Carotid Bifurcation

is accepted in partial fulfilment of the
requirements for the degree of
Master of Science

Date_____

_____
Chair of the Thesis Examination Board

Abstract

Ischemic stroke due to atherosclerotic disease has been studied widely in the recent past. Most studies focus on either the correlation between stroke risk and stenosis severity (narrowing of the plaque in the vessel) or mechanisms affecting platelet activation and aggregation. Shear stress has been identified as a strong indicator for platelet activation/aggregation, resulting in both thrombus formation and plaque growth. This has subsequently been correlated with regions of elevated turbulence.

Doppler ultrasound offers a method of characterizing these flow disturbances using a well-established parameter—turbulence intensity (TI), which is the root mean squared deviation in the spectral mean velocity. Using an in-house *in vitro* flow system, Doppler spectra are obtained at each of over 1000, 1-mm^3 isotropically spaced sites in the central plane of seven Teflon® phantoms simulating varying degrees of arterial disease. An average of TI over a 25 mm^2 region of interest, as well as the volume of TI and the cumulative TI over the internal carotid artery showed that downstream turbulence increased significantly with both stenosis severity (30% - 650% increase) and plaque asymmetry (10% - 30% increase).

Keywords: atherosclerosis, carotid artery, stenosis severity, plaque eccentricity, turbulence, volume, average, accumulation

Co-Authorship Statement

This thesis contains material that has been prepared for submission to a peer-reviewed journal. As such, it contains co-authored materials.

Chapter 2 presents material that has been prepared for submission to *Ultrasound in Medicine and Biology* as an original article entitled "Quantification of the Effects of Stenosis Severity and Symmetry on the Extent of Turbulence Intensity in Anthropomorphic Models of the Carotid Artery Bifurcation." This is co-authored by J.L. Powell, H.N. Nikolov, D.W. Holdsworth, R.N. Rankin and T.L. Poepping. I performed all experiments and analysis and wrote the manuscript for this work. T.L. Poepping has reviewed the results and the manuscript prior to submission. H.N. Nikolov was integral in experimental setup, manufactured all of the phantoms for the experiment and generated images for one of the figures for the manuscript. All co-authors will review final results and the manuscript before final submission.

Acknowledgements

There are many people I would like to acknowledge for their assistance with this work.

Firstly, I would like to thank Dr. Tamie Poepping for her countless hours spent reviewing, editing, and discussing my work.

I would also like to thank the members of my advisory committee: Dr. Jeff Hutter and Dr. Eugene Wong. They always had excellent questions and discussion about my research and made me really think about why I was doing what I was doing.

I would like to extend a huge amount of gratitude to Hristo Nikolov. He was always available to troubleshoot problems with the ultrasound system, and answer questions about my research in general. I don't think I would have made it through this project without his help.

I would also like to thank Dr. David Holdsworth for the use of both his lab space and ultrasound equipment for my experimentation.

I have great appreciation for my lab mates: Bushra Hussain, Sarah Kefayati, Emily Wong, Majid Yousif and Dr. David Tessier. Thank you all for keeping things light when they got to intense, for listening to me when I was stressed and for wonderful intellectual discussions that kept things interesting and making sense. I would like to

acknowledge the fourth year students who have passed through our lab, as well: Kwesi Agyem, Arvand Barghi, Sam Chippin, Dave Marchant, Peter McLachlan and Anna Rozik.

I would also like to thank Will Handler for his willingness to solve computer programming and software programs. There were certainly better ways he could have spent his time than explaining best coding practices to Physicists, but he never once complained.

Finally, I would like to thank my friends and family for all of their support through this long, arduous process. You guys never stopped believing in me and encouraging me, even when I did. For that, I will always be grateful.

Table of Contents

List of Figures

List of Abbreviations and Symbols

Alphanumeric Symbols

2D	Two dimensional
c	Speed of sound in material
D_d	Diameter of the distal internal carotid artery
D_s	Diameter of the internal carotid artery stenosis at the narrowest point
f_d	Doppler shifted frequency
f_r	Frequency of the sound pulse at the received by the ultrasound transducer
f_t	Frequency of the sound pulse at the received by the ultrasound transducer
l	Characteristic length (usually diameter of pipe)
r	Pearson-r correlation coefficient
Re	Reynolds number
v	Velocity of scatterers in the flow channel, as measured by the ultrasound probe
v_{mean}	Spectral mean velocity
v_{peak}	Spectral peak velocity
Z	Acoustic impedance

Greek Symbols

μ	Dynamic viscosity
ρ	Density

Units

cm	Distance to region of interest
cm/s	Mean velocity and turbulence intensity
$cm/s \cdot mm^3$	Cumulative turbulence intensity (spatial integral)
$cm/s \cdot mm^3 s$	Time integrated cumulative turbulence intensity
Hz	Ultrasound frequency parameters
kHz	Ultrasound frequency parameters
MHz	Ultrasound frequency parameters
mL/s	Flow rate
mm	Phantom length scale
mm^3	Volumetric size scale
ms	Temporal resolution scale

s	Cardiac cycle length scale

Acronyms and Multi-lettered Abbreviations

ADP	Adenosine diphosphate
ANOVA	Analysis of variance
BMF	Blood mimicking fluid
C30	30% concentrically stenosed model
C50	50% concentrically stenosed model
C70	70% concentrically stenosed model
CA	Carotid artery
CC	Cardiac cycle
CCA	Common carotid artery
CFD	Computational fluid dynamics
CE	Carotid endarterectomy
DUS	Doppler ultrasound
E30	30% eccentrically stenosed model
E50	50% eccentrically stenosed model
E70	70% eccentrically stenosed model
ECA	External carotid artery
ECG	Echocardiogram
ECST	European Carotid Surgery Trials
EDV	End diastolic velocity
ICA	Internal carotid artery
IV	Intravenous
MRI	Magnetic resonance imaging
NASCET	North American Symptomatic Carotid Endarterectomy Trials
PIV	Particle imaging velocimetry
PSV	Peak systolic velocity
RBC	Red Blood Cells
RMS	Root mean square
TI	Turbulence intensity
US	Ultrasound

Chapter 1 Introduction

1.1 Atherosclerosis

Atherosclerosis is a condition in which fatty material builds up in the wall of vessels causing the vessel wall to thicken and a deposit, generally referred to as a plaque, to build up (PubMed Health, 2011). This plaque buildup results in a narrowing of the residual vessel lumen area, which is commonly measured as a diameter reduction in planar images, where a circular cross-section of the vessel is assumed (Fox, 1993). Due to the complicated and varied composition of plaques (they often contain a variety of materials such as calcifications, lipids and cholesterol-esters), the vulnerability of the plaque, and the reaction to different flow stresses and drug treatments, is quite patient specific (Fuster, 1998). Because of this, atherosclerosis has been linked to a significant number of strokes (Taylor and Landau, 1990; White et al, 1996).

The carotid artery (CA) bifurcation is a common site for plaques; at this location, the common carotid artery (CCA) branches into the external carotid artery (ECA), which feeds blood to the fine vessels of the face and neck, and the internal carotid artery (ICA), which combined (there are two) provide approximately 80% of the total blood to the brain (Oktar, 2006). A common surgical prevention and intervention for stroke is carotid endarterectomy (CE). In this is a procedure, the common carotid artery (CCA) is clamped proximal (upstream) to the plaque and the internal (ICA) and external carotid arteries (ECA) are clamped distal (downstream) of any signs of plaque buildup. The CA is

then incised at the site of the bifurcation and the diseased portion of the vessel is removed. Finally, the vessel is closed and unclamped to return blood-flow to the downstream vasculature (Scott-Conner and Dawson, 2009). The invasive nature of CE, however, leads to a number of surgical risks (with 30 day risk rates), including disabling and non-disabling stroke (1.8% and 3.7% respectively) and death (1.1%); less severe symptoms, such as wound complications (9.3%) or anesthetic complications (0.8%) were also present (Ferguson et al, 1999).

In the last two decades, since carotid endarterectomy became commonplace, hospitalizations due to stroke have decreased from about 45 000 to about 14 000 Canadians annually (Public Health Agency of Canada, 2009). This suggests an improvement in stroke prevention, due to factors such as reduced smoking and better cholesterol and hypertension medications, in addition to the role of CE. An improvement in stroke management (i.e. the administration of patient care after the incidence of at least one stroke) was seen in the fact that the disparity between the total number of hospitalizations and the number of individual patients hospitalized for stroke each year has decreased steadily over this time period. However, while the number of stroke hospitalizations has decreased by about two thirds, the number of stroke deaths has only decreased by about a third (from 8500 to 5500 people) (Statistics Canada, 2010), suggesting that stroke is still a serious and financially costly disease. As such, there is still a further need for improvement in the early identification of those at greatest risk of stroke.

1.1.1 Clinical Trials to Assess the Role of Endarterectomy

Currently, stroke risk is assessed by the degree of narrowing (stenosis) in the ICA, just distal to the CCA bifurcation relative to the normal ICA lumen diameter, as seen in figure 1.1 (Fox, 1993). Equation 1.1 gives the numerical assessment for stenosis severity.

$$\% \, stenosis = \left(1 - \frac{D_s}{D_d}\right) \cdot 100\% \qquad (1.1)$$

Here, D_d is the diameter of the distal ICA and D_s is the diameter of the ICA at the narrowest part of the stenosis. This method of assessment was defined for consistency amongst centers in a large-scale clinical trial (the North American Symptomatic Carotid Endarterectomy Trial (NASCET)) that compared the degree of stenosis severity to the incidence of stroke in 1,212 patients with symptomatic carotid arterial disease to assess the effectiveness of carotid endarterectomy (NASCET Steering Committee, 1991). Additional results from the asymptomatic contra-lateral (opposite side) CAs were obtained from the same patients (Inzitari et al, 2000).

Until clinical trials such as NASCET and the European Carotid Surgery Trials (ECST) were performed, CE was arbitrarily performed as an alternative to the health risks of severe arterial disease. However, the risk-benefit tradeoff for the surgery was relatively unquantified, and thus was beginning to be questioned (Winslow et al, 1998). This is a highly invasive surgery that may in fact introduce more clots into the bloodstream due

to the endothelial damage at the surgical site (Rowed, 1986; Meyer, 1991; Bluestien et al, 2000). Based on these suspicions, large clinical trials were instigated.

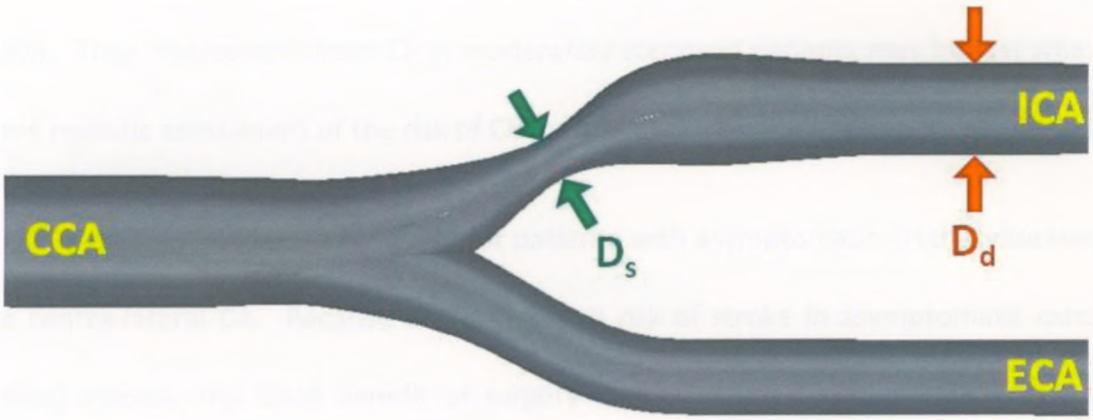

Figure 1.1: The assessment of stenosis severity according to NASCET standards in an idealized model of the stenosed carotid artery bifurcation. This assessment is performed in the internal carotid artery, and % stenosis is given by equation 1.1.

For both NASCET and ECST, patients with symptoms of carotid arterial disease were randomized into two groups: best medical treatment alone, and surgical treatment. Those patients in the surgical group received CE, while all patients received the best medical treatments as prescribed by their physicians and surgeons. Patients were then followed quarterly, and all adverse effects of both treatment options were reported, those being death and any type of stroke (NASCET Steering Committee, 1991). Risk of stroke was assessed at five years following inception into the study (Barnett et al, 1998).

Both NASCET and ECST showed that patients with severe carotid stenosis (> 70% stenosis by NASCET criteria or equivalent) had significantly improved risk-benefit ratio when undergoing CE compared to those receiving best medical treatment alone (Barnett, 1998; Warlow, 1993). There was a slight benefit from undergoing CE for

patients with moderate stenosis (50% - 69% stenosis by NASCET standards); however, these studies were performed using highly experienced surgeons with lower than average, pre-study history of CE risk (NASCET Steering Committee, 1991; Rothwell et al, 2003). Thus, the benefit from CE in moderately stenosed patients may be lost when a more realistic assessment of the risk of CE for less experienced surgeons is considered.

A further investigation was made for patients with asymptomatic arterial disease on the contra-lateral CA. Because of the reduced risk of stroke in asymptomatic carotid arterial disease, the small benefit of surgery that was seen for moderately stenosed vessels was lost (Inzitari et al, 2000). There was still some benefit gained by performing CE on severely stenosed asymptomatic vessels, but this was significantly reduced compared to the same benefit gained by patients with symptomatic vessels.

The risk of stroke due to ulceration was retrospectively studied by Eliasziw et al (1994) from angiographic assessment of plaque morphology. It was found that stroke risk in patients with ulcerated plaques increased from 26.3% in patients with 75% stenosis severity, to 73.2% in patients with 95% stenosis severity. This was compared to a constant 21.3% risk of stroke across the same range of stenosis severities in patients with non-ulcerated plaques.

It was concluded from these studies that high risk, symptomatic patients with severe carotid stenosis should receive carotid endarterectomy, but that caution should be taken in designating patients with less severe stenosis or asymptomatic vessels for CE as the risks could outweigh the benefits (Barnett et al, 1998). Also, the characterization of

risk based on stenosis severity alone has very low specificity; for NASCET (ECST), only 22% (17.1%) of symptomatic and 12% (5.7%) of asymptomatic patients with severe stenosis had a five-year (three-year) risk of stroke relative to a 12% (3.1%) risk of stroke after surgery (Barnett et al, 1998; Inzitari et al, 2000; ECST Collaborative Group, 1995).

1.2 Doppler Ultrasound

1.2.1 History and Fundamentals of Ultrasound

Ultrasound (US) has been used since its first medical applications in the late 1940s and early 1950s with early developments made by separate groups in the United States, Japan, Britain, Sweden, and Scotland (Goldberg and Kimmelman, 1988). These original designs were reflectoscopes, which collected a single A-line (amplitude of reflection) from the body; however, they had poor resolution. The common handheld transducers used in today's US systems were not developed until the mid to late 1960s (Goldberg and Kimmelman, 1988).

Ultrasound uses similar principles to sonar when detecting tissue and creating an image from this signal. A handheld transducer containing piezoelectric crystals (typically 128 or 256 segments) produces sound waves between 20 kHz and 20 MHz (well above the audible range) when an oscillating current is applied to the transducer (Gibbs et al, 2009). These sound waves are transmitted into the body, and reflections occur at points where there is a mismatch in acoustic impedance (Z), which is the product of the density of the material, ρ, and the speed of sound in the material, c (Szabo, 2004).

1.2.2 Continuous Wave and Pulsed Wave Doppler Ultrasound

For medical Doppler ultrasound (DUS) applications, a speed of sound of 1540 cm/s is used; this is the average speed of sound over all soft-tissues in the body (Ludwig, 1950). While the range for the speed of sound in the body is quite large, from 330 cm/s in air to 3400 cm/s in bone, the soft-tissue average is taken over body soft tissues, for which the range is much smaller: between 1430 and 1580 cm/s in fat and liver respectively (Hoskins et al, 2010). This range only leads to an error between the average value used for image construction and the actual value of the speed of sound of a maximum of 7%.

For continuous-wave DUS, velocity measurements are obtained in blood by taking advantage of the Doppler Effect. As seen in figure 1.2, red blood cells (RBC) travel through blood vessels with a velocity v. Incident US waves, with an incident frequency of f_t, will reflect off these cells and return to the transducer with a shifted frequency, f_r, where the change in frequency, f_d, is given by the Doppler equation (Middleton et al, 2004).

$$f_d = f_r - f_t = \frac{2 \cdot f_t \cdot v \cdot cos\theta}{c} \qquad (1.2)$$

From this, it can be seen that the received frequency, f_r, will be higher (i.e. the wave will be compressed) when the RBC has a velocity component towards the transducer ($v \cdot \cos\theta > 0$), while the received frequency, f_r, will be lower (i.e. the wave will be expanded) when the RBC has a velocity component away from the transducer ($v \cdot \cos\theta < 0$).

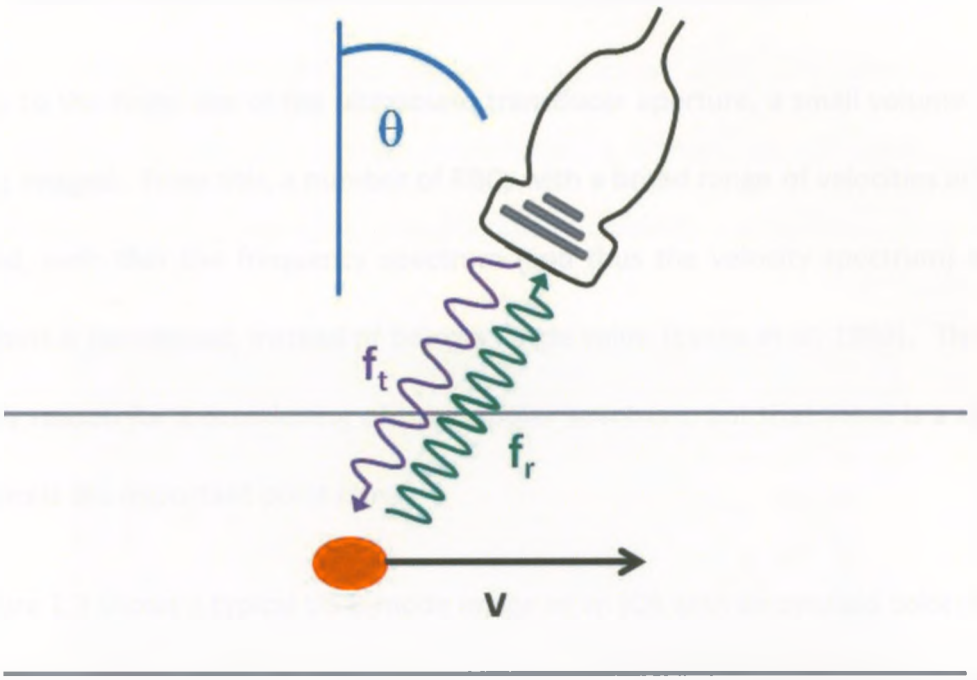

Figure 1.2: A schematic showing the assessment of Doppler ultrasound. The RBC (large red dot; not shown to scale) moving through the vessel has a velocity v. The transducer has a Doppler angle θ relative to the flow normal. The transmitted frequency, f_t (shown in purple), is incident on the cell, while the Doppler shifted signal with frequency f_r (shown in green) returns to the transducer with an altered frequency given by the Doppler equation (1.3).

Traditionally, the velocity of the flow would be obtained by rearranging equation 1.2 to solve for v. But in pulsed-wave DUS, the signal transmitted by the transducer is composed of multiple frequencies, creating a short-duration pulse (or burst) of signal with finite bandwidth. Due to the frequency-dependence of attenuation (which leads to higher attenuation of higher frequencies) the Doppler shift becomes distorted and difficult to discern. However, the motion of the RBC towards or away from the transducer results in a phase shift relative to the incident pulse due to the difference in the time of flight. It is this phase shift that is measured and converted into velocities in today's standard pulsed-wave DUS systems (Jensen, 1996).

1.2.3 Spectral Parameters and the Assessment of Stenosis Severity

Due to the finite size of the ultrasound transducer aperture, a small volume of fluid is being imaged. From this, a number of RBCs with a broad range of velocities are being sampled, such that the frequency spectrum (and thus the velocity spectrum) at each time point is broadened, instead of being a single value (Evans et al, 1989). This is not the only reason for a broadening of the Doppler spectrum, but that there is a range of velocities is the important point here.

Figure 1.3 shows a typical US B-mode image of an ICA with an overlaid color-Doppler map, and a corresponding DUS spectrogram (bottom) from the sample volume indicated by the oblique line. Typical velocity measurements have been calculated from the first cardiac cycle, separated by the thick, vertical white lines. Each shaded column in the spectrogram is a brightness (grey-scale) encoded representation of the spectral power as a function of frequency (or velocity) along the vertical axis and corresponds to a single time window (Gibbs et al, 2009). Displaying many of these consecutive spectral lines side-by-side as a function of time on the horizontal axis creates the spectrogram, which is generally displayed for several cardiac cycles. From each spectrum, features such as the spectral mean, v_{mean}, and peak, v_{peak}, velocities can be extracted and traced out on the spectrogram (Shung, 2006).

From this, different parameters that have been associated with stenosis severity, which in turn has been linked to stroke risk, can be extracted. Harward et al (1986) used spectral peak velocity to distinguish between mild, moderate and severe stenosis in 61

carotid arteries, but with only moderate sensitivity. Kimura et al (1998) had high sensitivity distinguishing moderate stenosis from other stenosis grades using peak systolic velocity (v_{peak} at peak systole, when velocity is maximal), but were unable to distinguish among highly stenosed, occluded and non-stenosed arteries.

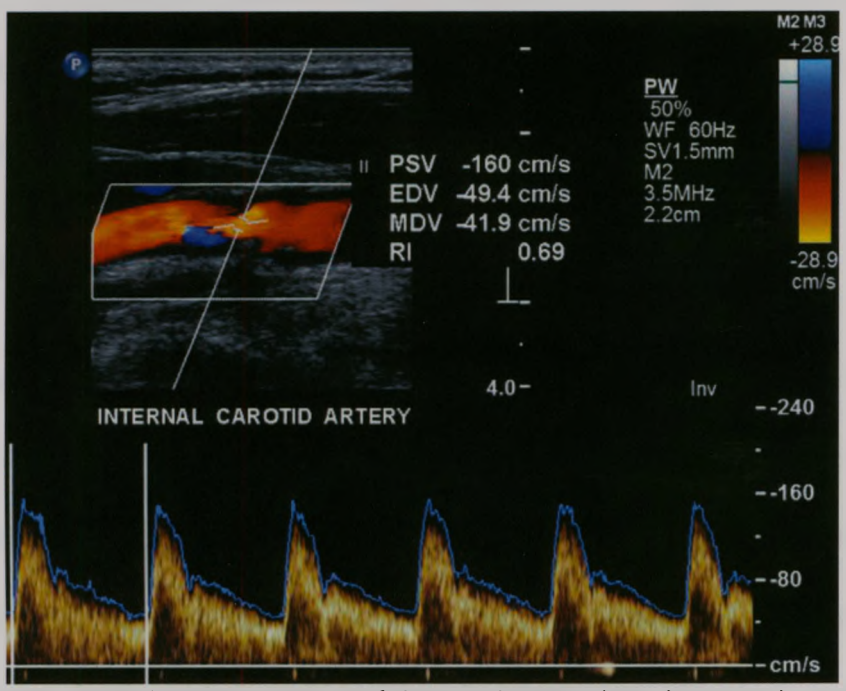

Figure 1.3: A traditional DUS scan image of the ICA showing the color- Doppler velocity map, superimposed on a B-mode image with a Doppler spectral display at the bottom. A single cardiac cycle is indicated by the thick white bars, and the blue line traces out the peak velocity over time, showing a peak systolic velocity (PSV) of 160 cm/s and end diastolic velocity (EDV) of 41.9 cm/s. It can be seen that the spectral broadening in this ICA is quite high, completely filling in the underside of the spectrum throughout the cardiac cycle, which corresponds well with the narrowing of the vessel seen in the color-flow image.
Source: http://www.healthcare.philips.com/

Further studies have looked at more complex parameters assessing flow from the DUS spectrum. Hutchison (1993) showed that the spectral shape was quite dependent on the flow type: the spectral shape was roughly Gaussian downstream of turbulence due to jet breakup, but was bimodal in the recirculation region where both forward and

reverse flow is seen. Rittgers et al (1983) assessed the degree of spectral broadening in 123 CAs and found that the spectrum tended to widen (the systolic window, or gap between 0 cm/s baseline and frequency signal, narrowed) with stenosis severity as measured in the distal (downstream) ICA. Kalman et al (1985) also looked at spectral broadening, but considered skewedness and kurtosis of the Doppler spectrum as well. They found that all of the parameters correlated well with stenosis severity in models perfused by simulated carotid waveforms.

1.3 Measuring Turbulence

Flow can be characterized as either laminar or turbulent. Laminar flow is described as smooth or orderly, where layers of flow are parallel and form laminae; a stream of dye injected in the flow will remain compact and unidirectional (Pope, 2000). When velocities increase or flow channel perturbations are introduced, the flow becomes more complex (with eddies and vortices forming) and disturbed, with eventual turbulence (McComb, 1990). In this case, random fluctuations in the velocity about its stable mean can be seen with the injection of a dye into the flow. Here, the dye will be dispersed considerably within a short distance as the flow disturbances mix the fluid layers together downstream of the injection site (Pope, 2000).

The Reynolds number (Re) is a dimensionless quantity, defined to classify flow according to the density, ρ, and dynamic viscosity, μ, of the fluid, the mean velocity of the fluid, v, and the characteristic length, *l*, of the flow channel (generally taken to be

the diameter). For a long straight tube with constant, well-developed flow running through it, Re is the ratio of inertial and viscous forces (Fox, 2004), which yields:

$$Re = \frac{Inertial\ Forces}{Viscous\ Forces} = \frac{\rho \cdot v \cdot l}{\mu} \qquad (1.3)$$

Laminar flow occurs for Re < 2300, while turbulent flow begins forming for Re > 4000 (Pope, 2000). Flow with intermediate Re is classified as being in transition; however, there is little agreement on the exact threshold between laminar and turbulent flow and this transition is not always defined (McComb, 1990; Furness, 1989). When flow conditions are less than ideal, for example there is wall roughness, a bifurcation, or a mesh or grid placed in the flow (as in the case of a fine mesh stent), turbulent flow can develop at much lower Re than would otherwise be expected (Bascom et al, 1993).

1.3.1 In Vitro Turbulence Devices

Traditionally, turbulence is measured experimentally using a hot wire anemometer, laser Doppler anemometry, and turbulence and pressure spheres. A hot wire anemometer works by measuring the change in resistance of a heated wire in a fluid resulting from a temperature change due to fluid flowing over the wire (McComb, 1990). Doing so provides very high spatial and temporal resolution measurement of the velocity in the flow and thus can provide accurate measurement of fluctuations in velocity in turbulent flow (Lomas, 1986). This fact makes wire anemometers the most common method of measuring velocity, and thus turbulence, in turbulent flow channels

(Rathakrishnan, 2007). Even though the wire is thin, the apparatus is often large and must be inserted perpendicular to the vessel. Also, the use of an electrically conductive wire is not practical within the body where electrical shock may occur. Thus, this is not a clinically feasible method of measuring turbulence.

Because of the wake fields generated behind blunt objects (Cannon et al, 1991), and the fact that they are computationally simple shapes, spheres are another common tool for measuring turbulence. Two types of spheres are often used: turbulence and pressure spheres. Both work on similar principles. With the turbulence sphere, a small sphere is placed in the fluid flow, and the velocity of the fluid is varied over a wide range (Rathakrishnan, 2007; Donelan and Motycka, 1978). From this, the drag force acting on the sphere can be determined accurately and the effective increase in Re due to the turbulence can be measured. Because a variation in the flow is needed, and the sphere is often quite large, the turbulence sphere is not suitable for either clinical or *in vitro* vascular flow measurements. The pressure sphere has small holes across its circumference such that it measures a pressure gradient across the sphere (Wesely et al, 1972). This device is only reliable under large amounts of turbulence due to external factors, such as fan blades or mesh grids, compounded with similar problems as the turbulence sphere (Rathakrishnan, 2007).

Laser Doppler anemometry works by using two intersecting laser beams reflecting off of particles within the flow. Due to the Doppler shift of moving reflectors, the returned signal will have a frequency shift relative to the initial signal. From this, a

measure of the velocity of the flow, and the resulting fluctuations about the mean, can be determined (McComb, 1990; Rathakrishnan, 2007). This method was used experimentally by Lesniak et al (2002) to investigate plaque irregularities in models of severely stenosed carotid bifurcations; however, no differences were seen between smooth and irregular models. Because this is an optical method, it requires transparent vessels and a transparent fluid, neither of which are present in the human body. Thus, it is suitable only for *in vitro* experimentation, not *in vivo* measurements in patients.

1.3.2 Clinically Applicable Devices

This work describes a technique for evaluating turbulence with the potential for translation to clinical applications. Both magnetic resonance imaging (MRI) and DUS provide clinically acceptable modalities with the capability of measuring blood flow and flow turbulence in the CA. Doppler ultrasound has an advantage over MRI of being far less expensive and is typically the front-line diagnostic tool for vascular measurements.

MRI has recently shown promise for the clinical detection of turbulence downstream of stenoses. Dyverfeldt et al (2006) showed a method of calculating the flow turbulence from the velocity distribution across a voxel, and relating this to turbulence. O'Brien et al (2009) were able to measure v_{peak} in turbulent jets with higher accuracy than was previously done by using an ultra-short radiofrequency pulse; this method could easily be extended to measurements of turbulence intensity using ensemble averaging.

Doppler ultrasound has a well-established role as a standard clinical tool, and its potential for measuring turbulence has been demonstrated both *in vitro* and *in vivo*. The effects of turbulent flow on the Doppler power spectra have also been investigated. Shung et al (1992) showed that turbulent flow tends to have a higher total backscattered power than is seen in laminar flow of the same flow rate. This was confirmed by Cloutier and Shung (1993), where a broadened spectrum was also seen in turbulent flow when compared to laminar flow of the same mean velocity. Wu et al (1998) showed similar results, where Doppler power was found to increase non-linearly with TI.

In contrast, Travis et al (2004) assessed a method of measuring turbulence *in vivo* using a technique that employs mean and peak velocity averaging. *In vivo* measurements were also made in pigs by Nygaard et al (1994), in which they measured Re stresses in the turbulent flow field two vessel diameters downstream of a 75% stenosis. Steinbruchel et al (1997) used DUS directly on the aorta immediately after the surgical implantation of a new type of aortic valve; they determined that the turbulence stress (a measure of the turbulence, the product of the square of turbulent velocity and fluid density, also known as Reynolds normal stress) in the ascending aorta was significantly lower downstream of the new valves when compared to turbulent stresses seen downstream of traditional artificial aortic valves.

The Doppler US signal can also be post-processed offline to assess turbulence. Two methods of analysis were previously demonstrated on carotid velocity data by Poepping

et al (2002) and Thorne et al (2010). These methods account for both the variability of velocity over the cardiac cycle due to the pulsatility of the heart (Holdsworth et al, 1999), and the need for a non-invasive measuring tool that can incorporate a clinically available imaging modality.

The first method, which is the method employed for this study, was introduced by Walburn et al (1983). Multiple cardiac cycles (CC) of DUS mean velocity data, obtained as described above, are considered from a single site in the vessel. Each individual CC is segmented out by its ECG-style (echocardiogram) gating signal and combined such that corresponding time points from all of the CCs coincide. The root-mean-square (RMS) deviation among the matched CC time points is defined as the turbulence intensity (TI), as seen in figure 1.4, and is a measure of the turbulence at that point in the flow. The deviation about the v_{mean} over all time points is not taken here because of the pulsatile nature of flow in the human body. Even in the most stable of flow conditions, this pulsatility would be measured as a significant turbulence intensity if fluctuations about an overall time-averaged mean were used.

The above method relies on an ECG signal to denote a consistent point within the CC for segmentation of the data into individual CCs. However, traditional US exams do not have ECG signals available, thus there is no reliable method to segment and align consecutive CCs with normal cycle length variability. Thus, another method was proposed that utilizes knowledge of the frequency content of the expected flow waveform, compared to that of the fluctuations due to randomized noise, turbulence

and cardiac variability. It is expected that the components of the Doppler signal associated with the flow waveform will be less than 12 Hz (Holdsworth et al, 1999); thus, taking a high pass filter of the signal to filter out those frequencies should leave only velocity fluctuations associated with velocity fluctuations. Thorne et al (2010) showed that turbulent flow fluctuations could be distinguished from other randomized fluctuations; this method does, however, have the disadvantage that it can only asses cycle averaged TI, whereas ensemble averaged TI can assess TI as a function of time within the cardiac cycle.

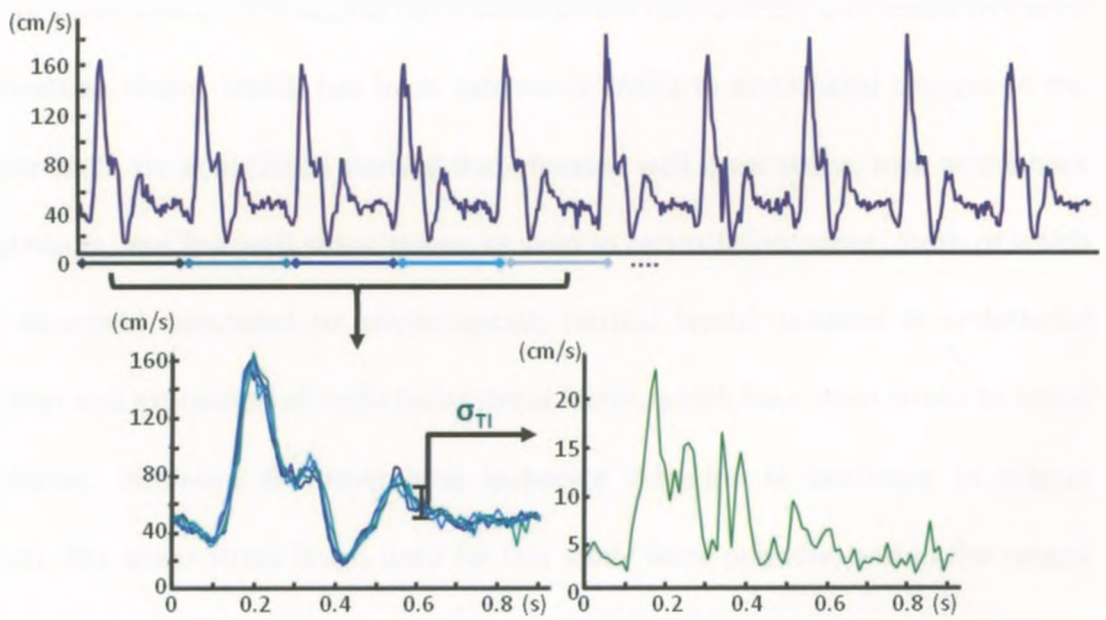

Figure 1.4: A schematic of the calculation of TI using the ensemble averaging technique described by Walburn et al (1983). The upper figure shows a tracing of ten consecutive cardiac cycles of data collected at a single site in the jet of a 70% concentric model. In the lower left figure, only the first five cardiac cycles have been shown to avoid clutter; however, all ten cycles would normally be used for analysis. The lower right figure shows the resulting TI trace as a function of the cardiac cycle.

1.4 Hemodynamics

The carotid artery bifurcation has been identified as a common site of plaque buildup due to complicated hemodynamics at this site (Ku, 1997). Mechanisms such as elevated shear stress and turbulence lead to cellular changes in both the blood stream and the vessel wall. This causes the region of the bifurcation to become vulnerable to vascular changes.

1.4.1 Wall Shear Stress

Wall shear stress, the frictional force between the fluid and the wall based on the no slip condition (Pope, 2000), has been commonly linked to endothelial changes in the vascular wall. Yin et al (2011) showed that elevated wall shear stress, seen at the neck of a stenosis, and low wall shear stress, as seen in recirculation zones, (both of which were abnormal compared to physiologically normal levels) resulted in endothelial activation and expression of endothelial tissue factor, which have been linked to blood coagulation, thrombus formation and leukocyte adhesion (a precursor to plaque buildup). The shear stress levels used for this study were pulsatile, and in the ranges seen physiologically for the vascular regions described.

An early model was developed suggesting that the permeability of the vessel wall through the endothelium was related to the wall shear stresses it was exposed to (Friedman and Fry, 1993). This model accounted for the changes in wall shear stress due to the progression of disease. A more recent model by Suh et al (2005) was

compared with clinical data for sites of atherosclerosis. This model showed that oscillatory wall shear stresses (resulting from abnormal forward and reverse flow) may play a key role in the development and progression of atherosclerotic plaques.

These models followed from work was done by Ku et al (1985) and Zarins et al (1983) showed a direct correlation between regions of abnormal wall shear stress and the development of atherosclerotic plaques. This first study found a correlation between the thickening of the intima-medial layer of the outer wall of the carotid sinus (the wall of the non-bifurcation side of the bulb of a non-stenosed ICA) and an index which the defined to account for the oscillating nature of the shear stress due to the pulsatile nature of the carotid flow waveform. The second study by Zarins et al (1983), shear stress was accurately measured using steady flow models and laser Doppler anemometry, while wall thickening was measured in human carotid artery samples obtained at autopsy. Again, it was found that thickening of the vessel walls occurred nearest to the bifurcation in the carotid sinus, on the opposite wall to the bifurcation; downstream, little thickening was seen, and what was present showed no preference for side on the vessel.

More recently, Beneli et al (2009) investigated endothelial changes in a more direct manner. For this study, 1.5mm diameter mushroom shaped plugs were inserted into the abdominal aortas of rats. Microscopy images revealed that, after 15 days, cells downstream of the plug, where a recirculation region would form, were enlarged and perpendicular to the flow, whereas endothelial cells on the top of the plug were

elongated in the direction of the flow. This same region developed a neointima layer that completely covered the plug within 30 days of surgery.

1.4.2 Free Shear Stresses

Free shear stresses, which are shear stresses between lamina in the blood with different velocities, also affect the hemodynamics within the vessel, primarily by activating the platelets in the blood. There are two mechanisms that result in platelet activation: contact with agonists, such as collagen receptors (released by the endothelium), adenosine diphosphate (ADP), epinephrine or thrombin (Davi and Patrono, 2007), or high shear stresses (Zannad and Stoltz, 1992). Agonists are released into the vessel by the vessel wall as a defensive tool to repair injury to the tissue (Gui et al, 2007). One such occurrence of injury is the rupture of an arterial plaque, in which activated platelets will both patch the ruptured site and create problematic platelets that can aggregate further downstream, possibly in the brain causing stroke (Offermanns, 2006).

Shear induced platelet activation also plays a key role in the activation of platelets. The narrowing of the artery causes the velocity through this stenotic neck to increase as the same amount of fluid must pass through a smaller channel (Ku, 1997). As platelets pass through the high velocity jet created by the narrowing at the site of stenosis, they experience high shear stresses (Gay and Zhang, 2009; Tang et al, 2002). This high shear stress has been linked to increased rates of activation (Hellums, 1993). However, the high velocity jet is not sustained, but rather it is pulsatile (it peaks and diminishes

throughout the cardiac cycle), which has been found to increase the rate of shear induced activation significantly (Ku et al, 1985).

The number of platelets that become activated has been linked to both the magnitude of shear and the duration that shear is applied. To account for this, Bluestein et al (1997) proposed a new parameter, the level of activation, as the product of exposure time and shear stress. This parameter has since been used to exhibit this co-dependence on both time and level of shear (Einav, 2004). Nobili et al (2008) showed an experimental application of this concept in which a longer duration of high shear in a pulsed shear experiment resulted in significantly more activated platelets than a shorter pulse duration with the same maximum shear and the same time interval between the beginning of each pulse. Jetsy et al (2003) also investigated the relationship between shear stress and exposure time and found that platelet activation was higher in a stenosed flow loop had higher platelet activation than a non-stenosed flow loop and increased with increasing length of stenosis when exposed to the same constant flow rate. The higher shear rate in the stenotic portion of tubing was implicated in the higher platelet activation seen in this experiment.

Once the platelets are activated, they form aggregates in regions of low shear stress, such as those found in the recirculation zone just distal to the stenotic jet (Ku, 1985; Gay and Zhang, 2009). These aggregates, along with their deposition on the vessel wall, have been shown to be larger in eccentric models than concentric models of the same stenosis severity (Tambasco and Steinman, 2003). It was also found that pulsatile shear,

as seen *in vivo*, is associated with higher aggregation than a steady shear rate of the same maximum magnitude (Mertin et al, 2000). It was shown by Reininger et al (1995), that the recirculation zone present in branched flow provided sufficient residence times (confirmed by Cao et al (1998)) to allow for thrombin-induced clot formation to build up in this area.

1.4.3 Turbulence

Turbulent flow has been shown to occur commonly at sites of bifurcations and stenoses, where vasculature is more complicated (Ku, 1997). Turbulence has been directly linked to the development of thrombus and the rupture of plaques at these vulnerable flow sites. Smith et al (1972) showed a three- to fivefold increase in thrombus mass due to the introduction of a turbulence causing device in flow studies in canines. Stein and Sabbah (1974) also considered flow studies in dogs, and showed that TI and thrombus weight both increase with Re, but only in turbulent flow. Stein and Sabbah (1976) also looked at turbulent flow in the human aorta and found that patients with aortic stenosis had prolonged turbulence, while those with normal aortic valves had small amounts of turbulence, but it more easily dissipated.

Khalifa and Giddens (1981) used laser Doppler anemometry to show turbulence downstream of a stenosed flow channel increased with the degree of stenosis. Wong et al (2009) showed that turbulence intensity increased with varying sizes and shapes of plaque ulcerations in 50% eccentrically stenosed models of the carotid artery bifurcation relative to a non-ulcerated model of the same geometry. Lesniak et al (2002)

investigated flow disturbances in carotid models downstream of both 80% and 90% stenoses, and found that the size and shape of the turbulent region changed due to the ulceration.

Loree et al (1991) demonstrated that turbulence downstream of severe stenoses (in vascular models) caused pressure drops at carotid arterial blood flow rates; these pressure changes were hypothesized to be the cause of plaque rupture. How et al (1994) used a flow experiment comparing two types of arterial grafts to show that, downstream of the graft producing more turbulence, a higher amount of thrombus and platelets were seen.

In the experiment described by Beneli et al (2009), implanted plugs simulating eccentric stenoses in rats and showed that, downstream of the plug, there were observable levels of turbulence seen in DUS exams, although no quantitative measure of this turbulence was obtained, which correlated to the development of large thrombus on the distal side of the plug.

1.4.4 Turbulence-Shear Combined Effects

It is unlikely the case that shear stresses and turbulence act independently on the flow to cause hemodynamic changes on the vessels. In fact many studies focus on disturbed shear stress or turbulent shear stress as symbiotic factors, where these are simply the shear stress measured in turbulent or disturbed flow regions. A common location for these hemodynamic parameters is the regions just distal to the stenosis (Ku,

1997), which has shown to be well correlated with platelet activation (Girdhar and Bluestein, 2008).

It was shown by de Bruyn et al (2003) that increased turbulence is linked to higher platelet activation, which is less responsive to traditional medical treatments than normal, shear activated platelets. A relative blood damage index was used by Nygaard et al (1992) to account for the exposure time to turbulent shear stresses downstream of heart valves; this parameter was seen to correspond with endothelial damage and lethal damage to cells in the blood, including the platelets. Yip et al (2006) showed that platelet activation downstream of the carotid bifurcation was higher in patients with severe stenosis than those without; the source of this elevated platelet activation was not cited in this case. Disturbed shear stresses have also been shown to influence the site selectivity of plaque formation and affect this plaque vulnerability (Cunningham and Gotlieb, 2005).

1.5 Objectives and Hypothesis

Ultrasound has been widely used as a surrogate measure of stroke risk; in fact, it is currently the front-line screening tool for assessing stroke risk based on stenosis severity. Those patients assessed to have a high risk of stroke will undergo CE, an invasive, potentially high risk surgery. While US has low specificity in predicting stenosis severity, and stenosis severity has low sensitivity in predicting stroke risk, DUS has the potential to rapidly implement clinical, low-cost screening of direct measures of

hemodynamics affecting stroke risk. Thus, a better indicator of stroke risk is highly desirable in detecting and preventing this costly disease before it occurs.

Turbulence has been directly linked to thrombus formation (Smith et al, 1972; Stein and Sabbah, 1974; Beneli et al, 2009). Furthermore, both turbulence and shear stress have been correlated to plaque formation and growth (Zarins et al, 1983; Cunningham and Gotlieb, 2005), as well as endothelial damage (Beneli et al, 2009), platelet aggregation (Mertin et al, 2000), and plaque vulnerability (Cunningham and Gotlieb, 2005; Loree et al, 1991;), likely leading to rupture. Thus, a measure of the turbulence downstream of a stenosed carotid artery may lead to a measure of stroke risk once clinical verification can be made.

The objectives of this work are:

(1) To assess the effect of stenosis severity and plaque asymmetry on the flow disturbances as measured by TI;

(2) To determine various measures of turbulences:

(2.1) a simple, clinically feasible measure that is computationally fast

(2.2) a more complex indicator that accounts for the volumetric extent of the turbulence as well as the magnitude throughout the volume

(3) To evaluate the correlation between different turbulence measures keeping clinical feasibility in mind.

Chapter 2 describes the study performed (using an *in vitro* flow facility and seven idealized carotid models) to measure TI downstream of the carotid bifurcation stenoses. Chapter 3 will summarize this work and provide suggestions for future work to expand upon these experiments.

1.6 References

Barnett HJM, Taylor DW, Eliasziw M, Fox AJ, Ferguson GG, Haynes RB, Rankin RN, Clagett GP, Hachinski VC, Sackett DL, Thorpe KE, Meldrum HE. Benefit of carotid endarterectomy in patients with symptomatic moderate or severe stenosis. N Engl J Med 1998; 339: 1415-1425

Bascom PAJ, Cobbold RSC, Routh HF, Johnston KW. On the Doppler signal from a steady flow asymmetrical stenosis model: effects of turbulence. Ultrasound Med Biol 1993; 19: 197-210

Beneli CT, Barbosa PF, Floriano EM, Abrea MA, Ramalho FS, Junio JE, Rossi MA, Ramos SG. Can eccentric arterial plaques alone cause flow stagnation points and favour thrombus incorporation? Int J Exp Path 2009; 90: 295-310

Bluestein D, Nui L, Schoephoerster RT, Dewanjee MK. Fluid mechanics of arterial stenosis: relationship to the development of mural thrombus. Ann Biomed Eng 1997; 25: 344-356

Bluestein D, Rambod E, Gharib M. Vortex shedding as a mechanism for free emboli formation in mechanical heart valves. J Biomed Eng: Transactions of the ASME 2000; 122: 125-134

Cannon S, Champagne F, Glezer A. Observations of large-scale structures in wakes behind axisymmetric bodies. Exp Fluids 1993; 14:447-450

Cao J, Rittgers SE. Particle motion within in vitro models of stenosed internal carotid and left anterior descending coronary arteries. Ann Biomed Eng 1998; 26: 190-199

Cloutier G, Shung KK. *Cyclic variation of the power of ultrasonic Doppler signals backscattered by polystyrene microspheres and porcine erythrocyte suspensions*. IEEE Trans Biomed Eng 1993; 40: 953962 (IEEE Log Number 9210788)

Cunningham KS, Gotlieb AI. The role of shear stress in the pathogenesis of atherosclerosis. Lab Invest 2005; 85: 9-23

Davi G, Patrono C. Platelet activation and atherothrombosis. N Engl J Med 2007; 357: 2482-2494

de Bruyn KMT, Zwartkruis FJT, de Rooij J, Asserman JWN, Bos JL. The small GTPase Rap1 is activated by turbulence and is involved in integrin alpha(IIb)beta(3)-mediated cell adhesion in human megakaryocytes. J Biol Chem 2003; 278: 22412-22417

Donelan MA, Motycka J. Miniature drag sphere velocity probe. Rev Sci Inst 1978; 49:298

Dyverfeldt P, Sigfridsson A, Kvitting J-PE, Ebbers T. Quantification of intravoxel velocity standard deviation and turbulence intensity by generalizing phase-contrast MRI. Magn Reson Med 2006; 56: 850-858

Einav S, Bluestein D. Dynamics of blood flow and platelet transport in pathological vessels. Ann N Y Acad Sci 2004; 1015: 351-366

Eliasziw M, Streifler JY, Fox AJ, Hachinski VC, Ferguson GG, Barnett HJM. Significance of plaque ulceration in symptomatic patients with high-grade carotid stenosis. Stroke 1994; 25: 304-308

European Carotid Surgery Trialists Collaborative Group. Risk of stroke in the distribution of an asymptomatic carotid artery. Lancet 1995; 345: 209-212

Evans DH, McDicken WN, Skidmore R, Woodcock JP. *Doppler Ultrasound: Physics, Instrumentation, and Clinical Applications*. Chichester: John Wiley & Sons, 1989

Ferguson GG, Eliasziw M, Baar HWK, Clagett GP, Barnes RW, Wallace C, Taylor DW, Haynes RB, Finan JW, Hachinski VC, Barnett HJM. The North American Symptomatic Carotid Endarterectomy Trial: surgical results in 1415 patients. Stroke 1999; 30: 1751-1758

Fox AJ. How to measure carotid stenosis. Radiology 1993; 186: 316-318

Fox RW, McDonald AT, Pritchard PJ. *Significant Dimensionless Groups in Fluid Mechanics*. In: Anderson W, ed. Introduction to Fluid Mechanics. 6th Ed. Hoboken, NJ: John Wiley & Sons Inc., 2004. pp. 284-286

Friendman MH, Fry DL. Arterial permeability dynamics and vascular disease. Atherosclerosis. 1993; 104: 189-194

Furness RA. *Historical Review and Flowmeter Classification*. In: Flanagan TP, ed. Fluid Flow Measurement. Essex, UK: Longman Group UK Ltd, 1989. pp. 1-6

Fuster V, Badimon JJ, Chesebro JH. Atherothrombosis: mechanisms and clinical therapeutic approaches. Vasc Med 1998; 3: 231-239

Gay M, Zhang LT. Numerical studies of blood flow in healthy, stenosed, and stented carotid arteries. Int J Num Meth Fluid 2009; 61: 453-472

Gibbs V, Cole D, Sassano A. *The Piezoelectric Effect; Types of Doppler Instrumentation in Diagnostic Imaging,* In: Wilson C, Jackson C, eds. Ultrasound Physics and Technology: How, Why and When. Edinburgh, UK: Elsevier Ltd, 2009. pp. 13-17; 78-88

Girdhar G, Bluestein D. Biological effects of dynamic shear stress in cardiovascular pathologies and devices. Expert Rev Med Devices 2008; 5: 167-181

Goldberg BB, Kimmelman BA. *Medical Diagnostic Ultrasound: A Retrospective on its 40th Anniversary*. New York, NY: Eastman Kodak Company, 1988

Gui T, Reheman A, Funkhouser WK, Bellinger DA, Hagaman JR, Stafford DW, Monahan PE, Ni H. In vivo response to vascular injury in the absence of factor IX: Examination in factor IX knockout mice. Thromb Res 2007; 121: 225-234

Harward TRS, Bernstein EF, Fronek A. Range-gated pulsed Doppler power frequency spectrum analysis for the diagnosis of carotid arterial occlusive disease. Stroke 1986; 17: 924-928

Hellums JD, 1993 Whitaker Lecture: Biorheology in thrombosis research. Ann Biomed Eng 1994; 22: 445-455

Holdsworth DW, Norley CJD, Frayne R, Steinman DA, Rutt BK. Characterization of common carotid artery blood-flow waveforms in normal human subjects. Physiol Meas 1999; 20: 219-240

Hoskins P, Martin K, Thrush A (eds.). *Diagnostic ultrasound: Physics and Equipment*. New York, NY: Cambridge University Press, 2010.

How TV, Marios Y, Guidon R, Black RA. Effect of geometric taper on thrombosis in vascular prosthesis: and ex-vivo study. J Biomater Sci Polym Ed 1994; 6: 111-122

Hutchison KJ. Doppler ultrasound spectral shape in the poststenotic velocity-field. Ultrasound Med Biol 1993; 19: 649-659

Inzitari D, Eliasziw M, Gates P, Sharpe BL, Chan BKT, Meldrum HE, Barnett HJM. The causes and risk of stroke in patients with asymptomatic internal-carotid-artery stenosis. N Engl J Med 2000; 342: 1693-1700

Jensen JA. *Estimation of blood velocities using ultrasound: a signal processing approach*. New York, NY: Cambridge University Press, 1996.

Jesty J, Yin W, Perrotta P, Bluestein D. Platelet activation in a circulating flow loop: combined effects of shear stress and exposure time. Platelets 2003; 14: 143-149

Khalifa AMA, Giddens DP. Characterization and evolution of post-stenotic flow disturbances. J Biomech 1981; 14: 279-296

Kimura K, Yasaka M, Wada K, Minematsu K, Yamaguchi T, Otsubo R. Diagnosis of middle cerebral artery stenosis by transcranial color-coded real-time sonography. AJNR Am J Neuroradiol 1998; 19: 1893-1896

Ku DN. Blood flow in arteries. Ann Rev Fluid Mech 1997; 29:399-434

Ku DN, Giddens DP, Zarins CK, Glagov S. Pulsatile flow and atherosclerosis in the human carotid bifurcation. Positive correlation between plaque location and low oscillating shear stress. Arterioscler Thromb Vasc Biol 1985; 5: 293-302

Lesniak B, Kaluzynski K, Liepsch D, Palko T. The discrimination of stenosed carotid bifurcation models with smooth and irregular plaque surface. Part I. Laser and ultrasound Doppler flow studies. Med Eng Phys 2002; 24: 309-318

Lomas CG. *Fundamentals of Hot Wire Anemometry*. Cambridge, UK: Cambridge University Press, 1986.

Loree HM, Kamm RD, Atkinson CM, Lee RT. Turbulent pressure-fluctuations on surface of model vascular stenoses. Am J Physiol 1991; 261: H644-H650

Ludwig GD. The velocity of sound through tissues and the acoustic impedance of tissues. J Acoust Soc Am 1950; 22:862-866

McComb WD. *The Semi-empirical Picture of Turbulent Shear Flow; Recent developments in the study of turbulence*. In: Brady JM, Cullen AL, Jones TV, Van Bladel J, Woods LC, Wroth CP, eds. The Physics of Fluid Turbulence. New York, NY: Oxford University Press, 1990. pp. 1-9; 88-99

Mertin M, Chow T, Hellums JD, Thiagarajan P. A new role for P-selecting in shear-induced platelet aggregation. Circulation 2000; 102: 2045-2050

Meyer FB, Meissner I, Fode NC, Losasso TJ. Carotid endarterectomy in elderly patients. Mayo Clin Proc 1991; 66: 464-469

Middleton WD, Kurtz AB, Hertzberg BS. Practial Physics. In: Thrall JH, ed. Ultrasound: The Requisites (2nd Ed). St Louis, MI: Mosby Inc, 2004. pp. 3-27

NASCET Steering Committee. North American Symptomatic Carotid Endarterectomy Trial: Methods, Patient Characteristics, and Progress. Stroke 1991; 22: 711-720

Nobili M, Sheriff J, Morbiducci U, Redaelli A, Bluestein D. Platelet activation due to hemodynamic shear stresses: damage accumulation model and comparison to in vitro measurements. ASAIO J 2008; 54: 64-72

Nygaard H, Giersiepen M, Hasenkam JM, Reul H, Paulsen PK, Rovsing PE, Westphal D. 2-Dimensional color-mapping of turbulent shear-stress distribution downstream of 2 aortic bioprosthetic valves in vitro. J Biomech 1992; 25: 429-440

Nygaard H, Hasenkam JM, Pedersen EM, Kim WY, Paulsen PK. A new perivascular multielement pulsed Doppler ultrasound system for in-vivo studies of velocity-fields and turbulent stresses in large vessels. Med Biol Eng Comput 1994; 32: 55-62

O'Brien K, Myerson S, Cowan B, Young A, Robson M, Freemasons N, Trust W, Fellowship S. Phase contrast ultrashort TE: a more reliable technique for measurement of high-velocity turbulent stenotic jets. Magn Reson Med 2009; 62: 626-636

Offermanns S. Activation of platelet function through G protein-coupled receptors. Circ Res 2006; 99: 1293-1304

Oktar SO, Yucel C, et al. Blood-Flow Volume Quantification in Internal Carotid and Vertebral Arteries: Comparison of 3 Different Ultrasound Techniques with Phase-Contrast MR Imaging. AJNR Am J Neuroradiol 2006; 27:363-369

Pennell D, Sechtem U, Higgins C, Manning W, Pohost G, Rademakers F, van Rossum A, Shaw L, Yucel E. Clinical indications for cardiovascular magnetic resonance (CMR): consensus panel report. Eur Heart J 2004; 25: 1940-1695

Poepping TL, Nikolov HN, Lee M, Holdsworth DW. An in vitro system for Doppler ultrasound flow studies in the stenosed carotid artery bifurcation. Ultrasound Med Biol 2002; 28: 495-506

Pope SB. *Turbulent Flows*. Cambridge, UK: Cambridge University Press. 2000

Public Health Agency of Canada. *Tracking Heart Disease and Stroke in Canada*. 2009.

PubMed Health. *Atherosclerosis*. A.D.A.M Inc. 2011: http://www.ncbi.nlm.nih.gov/pubmedhealth/PMH0001224/

Rathakrishnan E. Instrumentation, Measurements, and Experiments in Fluids. Boca Raton, FL: CRC Press, 2007

Reininger AJ, Reininger CB, Heinzmann U, Wurzinger LJ. Residence time in niches of stagnant flow determines fibrin clot formation in an arterial branching model: detailed flow-analysis and experimental results. Thromb and Haemost 1995; 74: 916-922

Rittgers SE, Thornhill BM, Barnes RW. Quantitative-analysis of carotid-artery Doppler spectral waveforms: Diagnostic-value of parameters. Ultrasound Med Biol 1983; 9: 255-264

Rothwell PM, Gutnikov SA, Warlow CP. Reanalysis of the final results of the European Carotid Surgery Trial. Stroke 2003; 34: 514-523

Rowed DW. Risks of Carotid Endarterectomy. Stroke 1986; 17: 848-852

Scott-Conner CEH, Dawson DL. *Operative Anatomy*. Philadelphia, PA: Lippincott Williams &Wilkins, 2009

Shung KK. *Diagnostic ultrasound: imaging and blood flow measurements*. Boca Raton, FL: Taylor & Francis Group, 2006

Shung KK, Cloutier G, Lim CC. *The effects of hematocrit, shear rate, and turbulence on ultrasonic Doppler spectrum from blood*. IEEE Trans Biomed Eng 1992; 39: 462-469 (IEEE Log number 9107166)

Smith RL, Blick EF, Coalson J, Stein PD. Thrombus production by turbulence. J App Physiol 1972; 32: 261–264.

Statistics Canada. *CANSIM Table 102-0529: Deaths, by cause, Chapter IX: Diseases of the circulatory system (I00 to I99), age group and sex, Canada, annual (number), 2000 to 2006*. Released May 4, 2010

Stein PD, Sabbah HN. Measured turbulence and its effect on thrombus formation. Circ Res 1974; 35: 608–614.

Stein PD, Sabbah HN. Turbulent blood flow in the ascending aorta of humans with normal and diseased aortic valves. Circ Res 1976; 39: 58–65.

Steinbruchel DA, Hasenkam JM, Nygaard H, Riis CME, Sievers HH. Blood velocity patterns after aortic valve replacement with a pulmonary autograft. Euro J Cardiothorac Surg 1997; 12: 873-875

Suh SH, Roh HW, Kim DJ, Kwon HM, Lee BK. Significance of hemodynamic effects on the generation of atherosclerosis. J Mech Sci Tech 2005; 19: 836-845

Szabo TL. *Introduction*. In: Bronzino J, ed. Diagnostic Ultrasound Imaging: Inside Out. Burlington, MA: Elsevier Academic Press, 2004. pp. 1-19

Tambasco M, Steinman DA. Path-dependent hemodynamics of the stenosed carotid bifurcation. Ann of Biomed Eng 2003; 31: 1054-1065

Tang DL, Yang C, Walker H, Kobayashi S, Ku DN. Simulating cyclic artery compression using a 3D unsteady model with fluid structure interactions. Comput Struct 2002; 80: 20-21

Taylor WC, Landau WM. Atherosclerosis and stroke. Ann Neurol 1990; 28: 108

Thorne ML, Rankin RN, Steinman DA, Holdsworth DL. In vivo Doppler ultrasound quantification of turbulence intensity using a high-pass frequency filter method. Ultrasound Med Biol 2010; 36: 761-771

Travis BR, Christensen TD, Smerup M, Olsen MS, Hasnkam JM. An in vivo method for measuring turbulence in mechanical prosthesis leakage jets. J Biomech Eng 2004; 126: 26-35

Walburn FJ, Sabbah HN, Stein PD. An experimental evaluation of the use of an ensemble average for the calculation of turbulence in pulsatile flow. Ann Biomed Eng 1983; 11: 385-399

Warlow CP. Symptomatic patients: the European Carotid Surgical Trial (ECST). J Mal Vasc 1993; 18: 198-201

Wesely ML, Tanner CB, Thurtell GW. An improved pressure-sphere anemometer. Boundary-Layer Meteorology 1972; 2: 275-283

White DB, Schneider JR, Hoffman KN, Size GP, Coats RW, Laubach M, Erikson EJ, Caprini JA, Golan JF. Association between carotid artery bifurcation disease and risk factors for atherosclerosis. Vasc Surg 1996; 30: 495-503

Winslow CM, Solomon DH, Chassin MR, Dosecoff J, Merrick NJ, Brook RH. The appropriateness of carotid endarterectomy. N Engl J Med 1988; 318: 721-727

Wong EY, Nikolov HN, Thorne ML, Rankin RN, Poepping TL, Holdsworth DW. Clinical Doppler ultrasound for the assessment of plaque ulceration in the stenosed carotid bifurcation by detection of distal turbulence intensity: a matched model study. Eur Radiol 2009; 19: 2739-2749

Wu SJ, Shung KK, Brasseur JG. In situ measurements of Doppler power vs. flow turbulence intensity in red cell suspensions. Ultrasound Med Biol 1998; 24: 1009-1021

Yin W, Shanmugavelayudam SK, Rubenstein DA. The effect of physiologically relevant dynamic shear stress on platelet and endothelial cell activation. Thromb Res 2011; 127: 235-241

Yip HK, Lu CH, Yang CH, Chang HW, Hung WC, Cheng CI, Chen SM, Wu CJ. Levels and value of platelet activity in patients with severe internal carotid artery stenosis. Neurology 2006; 66: 804-808

Zannad F, Stoltz JF. Blood rheology in arterial-hypertension. J of Hypertens 1992; 10: S69-S78

Chapter 2 Turbulence Intensity Measures in Models of the Carotid Bifurcation with Simulated Plaque Symmetry and Asymmetry using Clinical Doppler Ultrasound[†]

2.1 Introduction

Cerebrovascular disease is the third leading cause of death in Canada and the United States. In Canada alone, it affects over 50 000 people each year and results in over $3.5 billion in health care costs annually (Public Health Agency of Canada, 2009; Statistics Canada, 2010). Nearly 14 000 of these events are fatal (Statistics Canada, 2010), with only 10% of people recovering completely (Heart and Stroke Canada, 2011) and nearly 320 000 people currently struggling with the consequences of previous cerebrovascular events (Dai et al, 2009). It is thus imperative that researchers seek new and effective methods for early, non-invasive assessment of stroke risk.

Clinically, the front-line assessment of carotid vascular disease uses Doppler ultrasound (DUS). A combination of peak systolic velocity (PSV – the maximum velocity at peak systole), peak end diastolic velocity (EDV – the maximum velocity at the end of diastole, the steady, low velocity region, just prior to the upstroke of systole (Bowman et al, 2009)), the ratio of PSV/EDV and a qualitative version of spectral broadening (the width of the spectral velocity components at a single time point) (Rittgers et al, 1983;

[†] A version of this chapter has been prepared for submission to *Ultrasound in Medicine and Biology* as an original article entitled "Quantification of the Effects of Stenosis Severity and Symmetry on the Extent of Turbulence Intensity in Anthropomorphic Models of the Carotid Artery Bifurcation" by J.L. Powell, H.N. Nikolov, D.W. Holdsworth, R.N. Rankin and T.L Poepping.

Barnes, 1991; Mays et al, 2000) are typically used as a surrogate measure of stenosis severity. These are measured at the jet through the neck of the stenosis where maximum velocity can be found on color Doppler, in the proximal common carotid artery (CCA) as a baseline measurement, and in the distal internal carotid artery (ICA). Unfortunately, these measures are often clinic- and machine-specific, angle dependent (Tola and Yurdakul, 2006) and have high inter-operator variability (Perrin et al, 1977; Srinivasan et al, 1995). Furthermore, the spectral capabilities of Doppler ultrasound are typically not being utilized to their full potential, with only peak, v_{peak}, and mean, v_{mean}, velocity being extracted, while the spectral shape is ignored or the distribution of the velocities is ignored or dismissed (Barnes, 1991).

Following large clinical trials of patients with symptomatic carotid arterial disease, it was determined that the two- and five-year risks of stroke in patients with severe stenosis of the ICA are significantly reduced for patients who undergo the surgical removal of the plaque (carotid endarterectomy) relative to those who receive best non-surgical treatment alone (Barnett et al, 1998; Warlow, 1993). However, the risk of stroke in patients with moderate stenosis severity (50-69% stenosis) is only mildly improved with carotid endarterectomy (Barnett et al, 1998; Ferguson et al, 1999). The risk in patients who have asymptomatic carotid disease have a negligible improvement when carotid endarterectomy is performed (Inzitari et al, 2000). This mild improvement in stroke risk is lost when it is corrected for other risk factors such as micro-emboli and ulcerations (Spence, 2010). It is suggested that stenosis severity alone is not a specific indicator of stroke risk.

More recent findings showing that only 11.2% of hospital-reported strokes are attributable to pre-cerebral stenosis or occlusion, a rate lower than the 15.9% of cerebral events that are transient ischemic events (Public Health Agency of Canada, 2009), further supporting the assertion that stenosis severity is not a specific indicator of stroke risk. Similar results were seen previously during the NASCET trials (Barnett et al, 2000; Inzitari et al, 2000) in which it was concluded that as many as 45% of ischemic strokes did not originate from the carotid arteries. Also, patients that have strokes due to stenosis or occlusion of the pre-cerebral arteries alone have hospital stays less than half as long as the average stay (7.1 vs. 16.8 days) (Public Health Agency of Canada, 2009). These facts would suggest that hemodynamics and the resulting thrombi, more than stenosis severity alone, affect the risk and effect of stroke in the majority of patients.

It has been well established that bifurcations are common sites of disease, and it is believed that it is the hemodynamics at the bifurcation that causes the development of plaque and the ejection of thrombus (Constantinides, 1990; Hellums, 1994; Jackson et al, 2009). Studies have shown that vessels with increased turbulence had a significantly increased mass of thrombus formation distal to the site of turbulence (Smith et al, 1972; Stein and Sabbah, 1974). The development of a well-controlled, model-based *in vitro* system allows for careful, systematic study of flow parameters with disease progression and symmetry of plaque buildup. Using such a system, Poepping et al. (2002) showed qualitatively that flow patterns vary significantly between different stenosis symmetries, and that flow disturbances are greatly exaggerated with increased stenosis severity.

Recently, stroke research has focused on more specific indicators of stroke, beyond stenosis severity. Much of this work has centered around the wall and free shear stresses involved in the activation of platelets to a sufficient level necessary for aggregation (Einav and Bluestein, 2004; Cunningham and Gotlieb, 2005; Raz et al, 2007; Chow et al, 2000). Other groups focused more on wall thickening, and the mechanisms associated with this (Van Popele et al, 2001; Chambless et al, 1997). Ku (1997) describes the flow characteristics within a diseased vessel, along with its association to both shear and the development of thrombosis. Wong et al (2009) have shown plaque ulcerations cause a significant increase in downstream flow disturbances.

Turbulence intensity (TI), the root-mean-square (RMS) deviation in the ensemble mean velocity, is a common measure of flow disturbances used in engineering applications. The volume of elevated TI is proposed here as an advanced measure of how disturbed the flow is in the vessel, as it is a measure of the extent of the flow disturbances, thus it is a potential indicator of risk of thrombus formation and consequently stroke. It is hypothesized that both stenosis severity and plaque eccentricity will affect the downstream flow disturbances as quantified by DUS TI suggesting that stenosis severity is not an independent risk factor for stroke.

2.2 Methods

2.2.1 In Vitro Data Collection System

An *in vitro* flow system was used (Poepping et al, 2002), which incorporates a clinical DUS system (HDI 5000, Philips-ATL, Oceanside, CA, USA), a computer-controlled flow pump (Compuflow 1000, Shelley Medical, Toronto, ON, Can) (Holdsworth et al, 1991), and anthropomorphic flow phantoms (Wong et al, 2008) with downstream resistance to simulate the peripheral vasculature. The pump perfuses the flow phantoms with a modified water-glycerol based blood-mimicking fluid (Ramnarine et al, 1998; Thorne et al, 2008) using a flow waveform, shown in Fig. 2.1, representing an idealized human carotid flowrate waveform (Holdsworth et al, 1999) with a 0.92 s cardiac cycle, peak flowrate of 23.46 ml/s, and mean flow rate of 6.000 ml/s.

A three-axis translational stage enables raster scanning of the ultrasound transducer across the phantom, with ECG-gated data collection at each of over 1000 sites in the central plane of the phantom with 1-mm homogeneous spatial resolution. This dataset comprises an 8 cm length of the carotid artery, beginning approximately 4.5 cm proximal to the apex of the bifurcation and extending approximately 3.5 cm distal to the apex. The central plane divides the center of the vessel through the diameters of the CCA, ICA and external carotid artery (ECA).

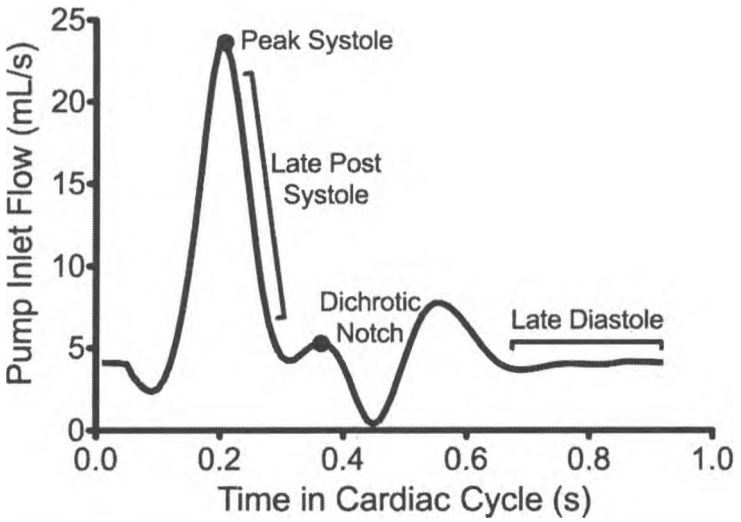

Figure 2.1: Pump flow waveform, showing key time points in the cardiac cycle, such as peak systole (the point of maximum flow), post systole (the down slope following peak systole during which the TI is typically maximal), the dichrotic notch (the point of local maximal flow prior to minimal flow before diastole), and the long period of late diastole in which low-velocity, sustained flow is generally seen.

Data were collected using a commercial ultrasound system (HDI 5000, Philips-ATL, Oceanside, CA, USA) with a 4-MHz linear array transducer (L7-4, Philips-ATL, Oceanside, CA, USA) focused at depth of 2.3 cm with a minimal sample-volume length of 1 mm. A pulse repetition frequency between 10 000 and 16 667 Hz was selected to prevent aliasing in the regions of maximum velocity (i.e. the jet of the ICA). The lowest possible wall filter of 50 Hz was applied, which is sufficient with the lack of wall motion in the rigid Teflon® phantoms. Ten seconds of dual-channel (forward and reverse) Doppler audio data were digitized at 44.1 kHz and recorded for off-line analysis.

A collection of seven phantoms was investigated for this experiment. The family of models shown in Fig. 2.2, representing serial progression of atherosclerotic plaque buildup in the carotid bifurcation, was based on models previously developed from an *in*

vivo angiographic characterization study (Smith et al, 1996) and were fabricated by milling complementary (mirrored) halves of the vessel from sheets of Teflon® polymer plastic and sealing these together using a silicone-based sealant as described in Wong et al (2008). Models simulate the progression of disease from a normal (disease-free) carotid to mild (30%, as characterized by NASCET criteria) (NASCET Steering Committee, 1991), moderate (50%), and severe (70%) stenosis, due to plaque formation just distal to the bifurcation on the inlet of the ICA. The diseased models incorporate two series of plaque progression: one based on symmetric (concentric) plaque buildup and the other with asymmetric (eccentric) plaque buildup on the non-flow-divider side of the ICA.

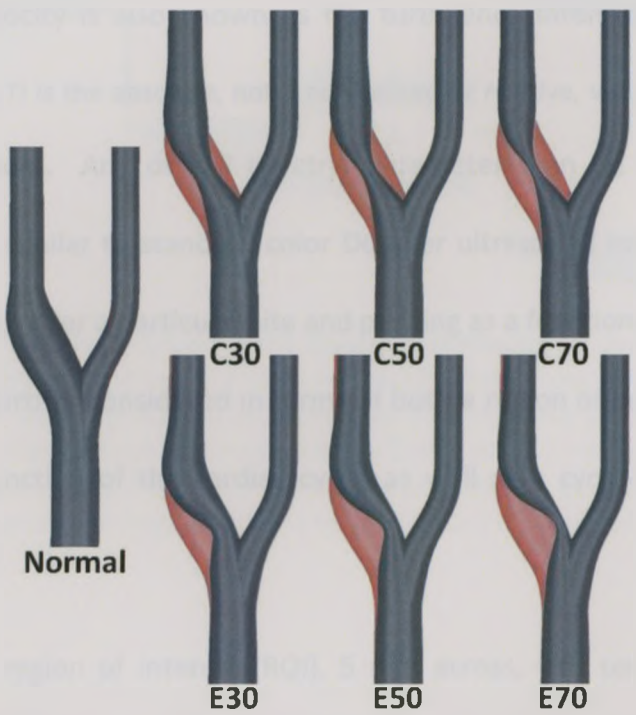

Figure 2.2: The family of seven anthropomorphic models of the carotid artery demonstrates progressive plaque buildup (shown in underlying red). For each model, the CCA (bottom) branches into the ICA (left branch) and external carotid artery (ECA, right branch). On the left, the normal, or disease-free, model shows the baseline upon which all the others are based. The concentric models with 30% (C30), 50% (C50) and 70% (C70) show the progression of increasing symmetric plaque buildup; similarly the eccentric models show the progression of asymmetric plaque buildup for 30% (E30), 50% (E50) and 70% (E70) stenoses.

2.2.2 Offline Data Analysis

Offline analysis was performed on the data from each site using a 1024-point FFT, with a Hanning window and 50% overlap between consecutive windows, to extract a Doppler spectrum from the audio data every 12 ms. From this, key spectral parameters were extracted, such as spectral mean and peak velocities, spectral width, and integrated power. Next, an ensemble average was performed by aligning the 10 consecutive cardiac cycles, based on cardiac-gating and known cardiac cycle length, allowing calculation of the ensemble average and RMS deviation for each time point in the cardiac cycle (Poepping et al, 2002). Note that the RMS deviation in the ensemble averaged mean velocity is also known as the turbulence intensity. It is important to distinguish here that TI is the absolute, not a normalized or relative, value as is often used for engineering applications. Any of the spectral parameters can be visualized as color-encoded 2D maps, similar to standard color Doppler ultrasound images used clinically, or by extracting values for a particular site and plotting as a function of the cardiac cycle. In this study, TI is further considered in terms of both a region of interest and a volume of interest, as a function of the cardiac cycle, as well as a cycle-integrated value, as shown in figure 2.3.

First, a square region of interest (ROI), 5 mm across, was considered in the ICA, centered 1.5 cm (approximately 2 CCA diameters) distal to the bifurcation. This region is shown in figure 2.4. The turbulence intensity was averaged over the ROI, and the experiment was repeated five times to estimate the variability in the TI over the ROI. A

single time point was extracted to show the trend in the data with increasing stenosis severity, as well as the difference between concentric and eccentric geometries with the same level of disease (% stenosis severity). This time point corresponded to the time point of maximum average TI in the ROI; the maximum time was not assumed to be the same for each model.

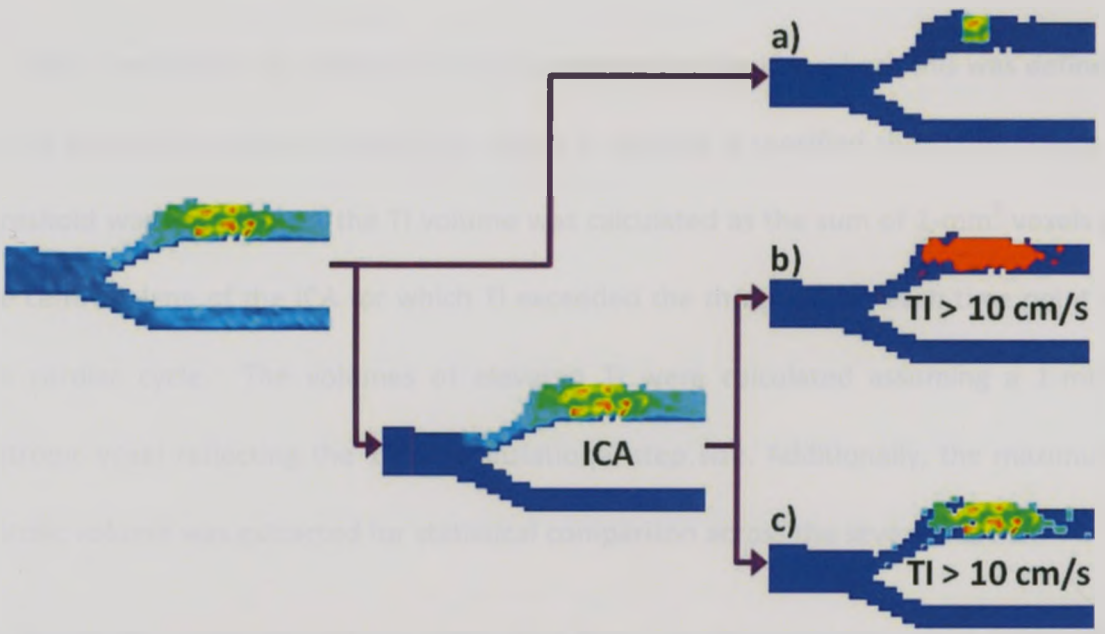

Figure 2.3: Schematic of the selection of the different parameters for measuring TI in the ICA of the E50 model. First, a region of interest is selected from the color plot of TI a) yielding the ROI averaged TI. Next, the ICA can be segmented from this color plot, and the spatial points exceeding a threshold can be considered as a binary map b), yielding the volume of elevated TI, or as their values of TI c). Integrating the remaining TI values in this last plot over space reveals the cumulative elevated TI for a single time point in the cardiac cycle.

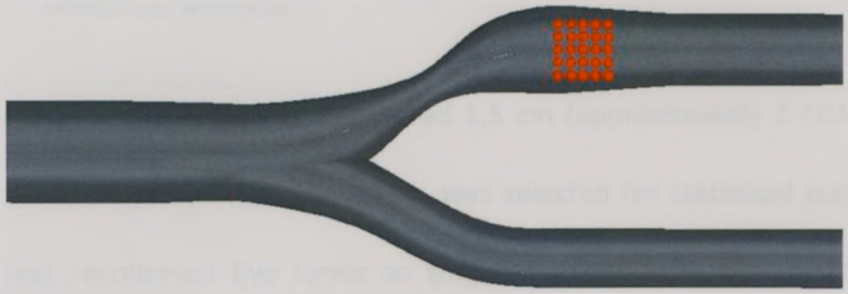

Figure 2.4: The region of interest outlined in the ICA of the 50% concentric model. The same region was used in all models; however, only one model is shown here.

Next, the volume of *'elevated TI'* was considered in the ICA, where this was defined as the volume (i.e. sum of voxels) for which TI exceeds a specified threshold. Once a threshold was determined, the TI volume was calculated as the sum of 1-mm^3 voxels in the central plane of the ICA for which TI exceeded the threshold for each time point in the cardiac cycle. The volumes of elevated TI were calculated assuming a 1-mm^3 isotropic voxel reflecting the 1-mm translational step size. Additionally, the maximum systolic volume was extracted for statistical comparison across the seven models.

Finally, the *cumulative TI* was defined as the sum of elevated TI values across the volume of interest (i.e. the ICA) or alternatively the TI-weighted volume of elevated TI. This was calculated as the sum of the TI values over all voxels (i.e. the discrete spatial integral of TI), across the central plane of the ICA, for which TI exceeded the specified threshold value for each time point in the cardiac cycle. Again, the time point of maximal cumulative TI for each model was extracted to more closely examine any differences between the seven models. Also, the integral of cumulative TI over a cardiac cycle was considered for each model for comparison to the time-averaged clinical results presented by Thorne et al (2010).

2.2.3 Statistical Analysis

A square ROI, 5 mm across and centered 1.5 cm (approximately 2 CCA diameters) downstream of the apex of the bifurcation, was selected for statistical purposes. This sub-region was recollected five times so that, combined with the same sub-region selected from the original collection of the entire central plane, statistical analysis can be performed on six data sets (a selection from the central plane, plus the five repeated measurements) of the ROI. The standard deviation in the mean TI in the ROI from the 6 trials (i.e. repeated measures variability) was taken as the error in the measurement for all statistical analysis.

The exception was the eccentric 30% model for which only a single trial was successfully obtained. In this case the standard error (the standard deviation divided by the square root of the number of points) in the 25 points across the ROI was used as an approximation of the error in the repeated measures data used in the other geometries. This was found to be an over estimation of the error in other models assessed with repeated measures, so would not introduce any false statistically significant results.

Because two independent variables (percent stenosis severity and eccentricity) are being compared, a two-way ANOVA (analysis of variance) was performed. A Bonferroni post-hoc test for multiple comparisons was applied, both to pair-wise compare the concentric models against eccentric models with the same stenosis severity (McDonald, 2009), and to determine if differences existed between different stenosis severities with

the same eccentricity (Glantz, 2009). All analyses were performed using a commercially available statistical software package, Prism (GraphPad Software Inc, La Jolla, CA, USA).

2.3 Results

2.3.1 2D color-encoded DUS parametric maps

Figures 2.5 and 2.6 show 2D color-encoded maps of v_{mean} and TI in the central plane during late systole (35 ms following peak systole, t=233 ms on Fig. 2.1). These help to demonstrate the formation of the recirculation zones and flow disturbances during flow deceleration, in all seven models. The v_{mean} map is similar to a typical color-Doppler ultrasound image, which is readily available on commercial ultrasound systems. However, at present, there is no equivalent determination or display of TI available on commercial ultrasound systems.

It can be seen qualitatively that the complex flow regions in the v_{mean} map, where forward and reverse flows combine to create vortices, are represented by elevated levels of TI in the corresponding geometries of the TI images. These show up in areas of flow disturbances, as well as recirculation regions and with the downstream dissipation of the high velocity jet. Also notable is the qualitative increase in the magnitude of the TI with increasing stenosis severity for both the concentric and eccentric models, ranging from 2-4 cm/s in the normal model, through 5-15 cm/s in the 30%, 10-25 cm/s in the 50%, and 25-45 cm/s in the 70% models. It also appears that the area covered by the elevated TI is higher for the eccentric models in both the 30% and 50% cases than

the corresponding concentric models of the same stenosis severity, which is quantitatively assessed below.

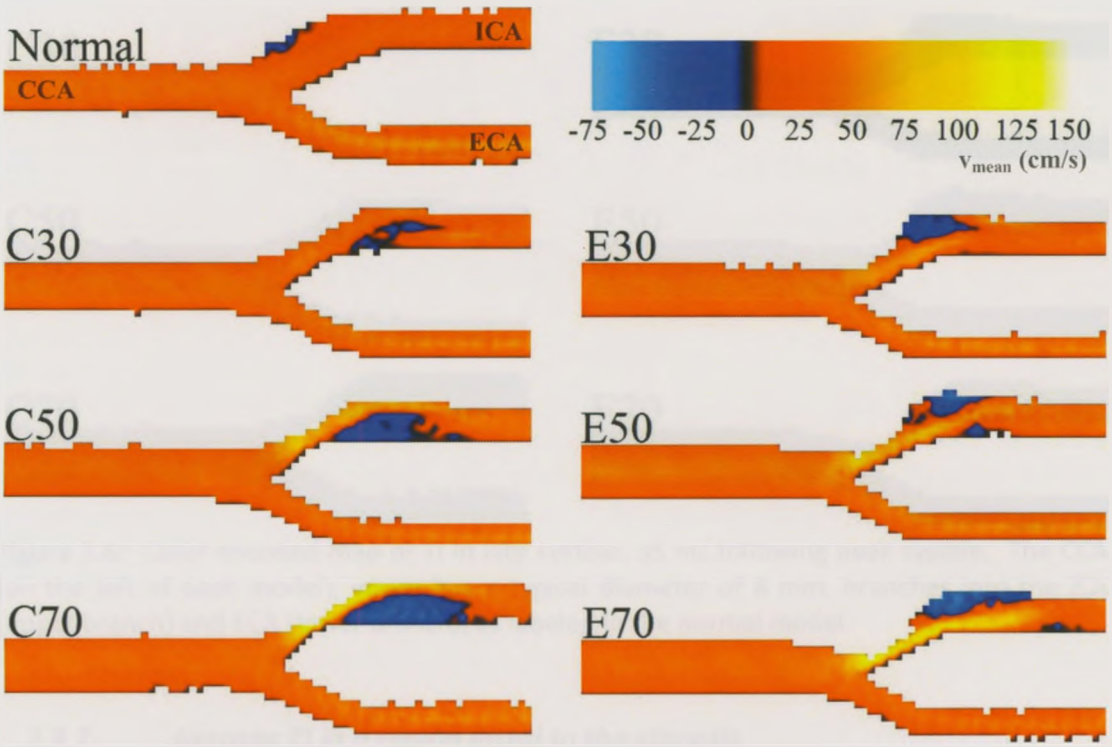

Figure 2.5: Color encoded map of v_{mean} in late systole, 35 ms following peak systole. The CCA (on the left of each model), which has a typical diameter of 8 mm, branches into the ICA (upper branch) and ECA (lower branch), as labeled in the normal model.

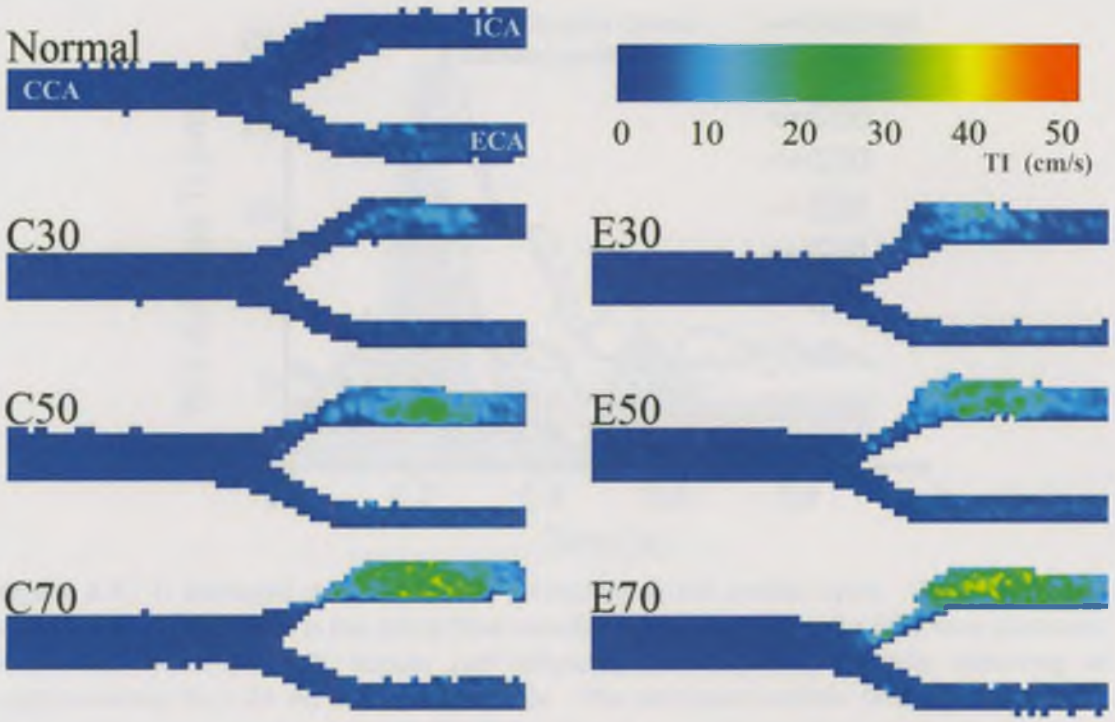

Figure 2.6: Color encoded map of TI in late systole, 35 ms following peak systole. The CCA (on the left of each model), which has a typical diameter of 8 mm, branches into the ICA (upper branch) and ECA (lower branch), as labeled in the normal model.

2.3.2 Average TI in a region distal to the stenosis

Figures 2.7 and 2.8 show the average TI in a 25-mm^2 region of interest in the ICA 1.5 cm (~2 CCA diameters) distal to the apex of the bifurcation. Figure 2.7 shows the average TI in this ROI as a function of the cardiac cycle, demonstrating increasing TI with increasing stenosis severity, primarily during periods of fluctuating flow rate, particularly the decelerating phase of systole. Additionally here, the average TI is higher for the eccentric models as compared to their concentric counterparts in both the 30% and 50% stenosed models. This is further demonstrated in Fig. 2.8 showing the average TI in the ROI at the time point of maximum TI for each model (0-47 ms following peak systole, depending on the model).

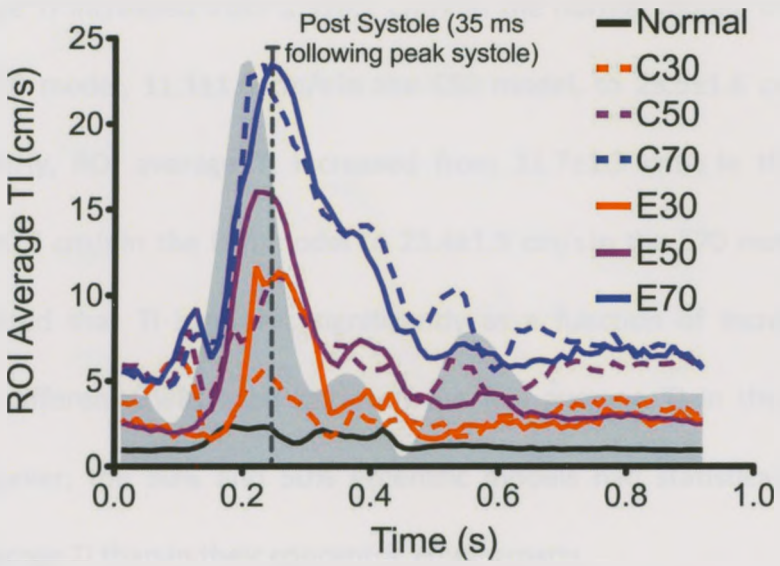

Figure 2.7: TI averaged over the ROI as a function of the cardiac cycle. The grey shaded region in the background is the pump flow waveform, visualized here for reference purposes. Maximum TI in the ROI occurs just following peak systole, typically occurring at approximately 35 ± 24 ms after peak systole. This post-peak-systolic time point has been indicated by the dashed, vertical line.

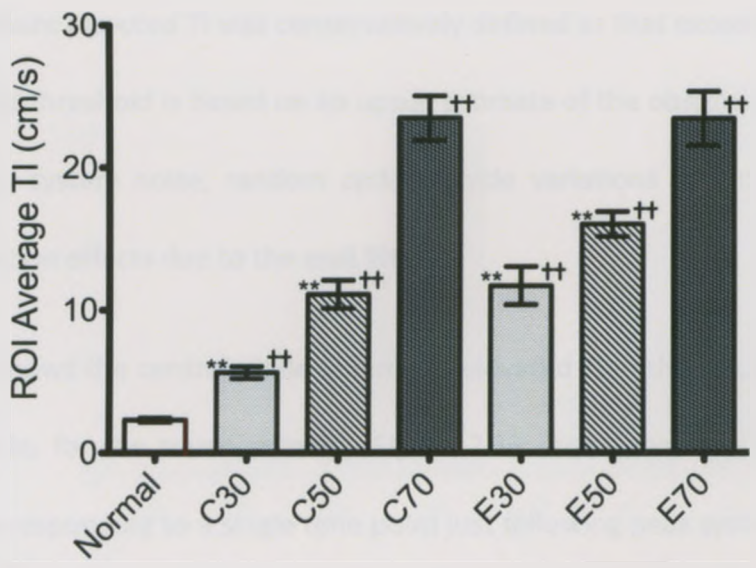

Figure 2.8: Average TI in the ICA ROI at the time of maximal TI in each model. An asterisks (*) on the left side of the bar indicates a statistically significant difference between that model and the corresponding model of the same stenosis severity, but opposite stenosis symmetry. A cross (†) on the right side of the bar indicates that there is a statistically significant difference between that model and the next less stenosed model of the same eccentricity. Here, differences were statistically significant at a level of $p<0.01$ based on a two-way ANOVA and Bonferroni post-hoc test. Error bars represent standard deviation in the repeated trials, as described in section 2.2.3.

ROI average TI increased from 2.3±0.2 cm/s in the normal model, through 5.6±0.4 cm/s in the C30 model, 11.1±1.0 cm/s in the C50 model, to 23.5±1.6 cm/s in the C70 model. Similarly, ROI average TI increased from 11.7±1.3 cm/s in the E30 model, through 16.0±0.9 cm/s in the E50 model to 23.4±1.9 cm/s in the E70 model. Statistical analysis indicated that TI increases significantly as a function of increasing stenosis severity. No difference was seen between the ROI average TI in the C70 and E70 models. However, the 30% and 50% eccentric models had statistically significantly higher ROI average TI than in their concentric counterparts.

2.3.3 Central-plane volume of elevated TI in the ICA

For each model, the volume of elevated TI in the central plane of the ICA was determined, where *elevated* TI was conservatively defined as that exceeding a threshold of 10 cm/s. This threshold is based on an upper estimate of the observed background TI associated with system noise, random cycle-to-cycle variations in the flow, and low-velocity fluctuation effects due to the wall filter.

Figure 2.9 shows the central-plane volume of elevated TI in the ICA, as a function of the cardiac cycle, for the seven models. Figure 2.10 shows the maximum volume of elevated TI, corresponding to a single time point just following peak systole, as indicated by the horizontal dashed line in Fig. 2.9. For most models, the maximum TI occurred at 35±12 ms after peak systole. An exception was a TI spike in the concentric 30% model, near the time of the dichrotic notch, which could be traced to spuriously high TI values arising from very low velocities along the wall fluctuating around the wall-filter cut-off.

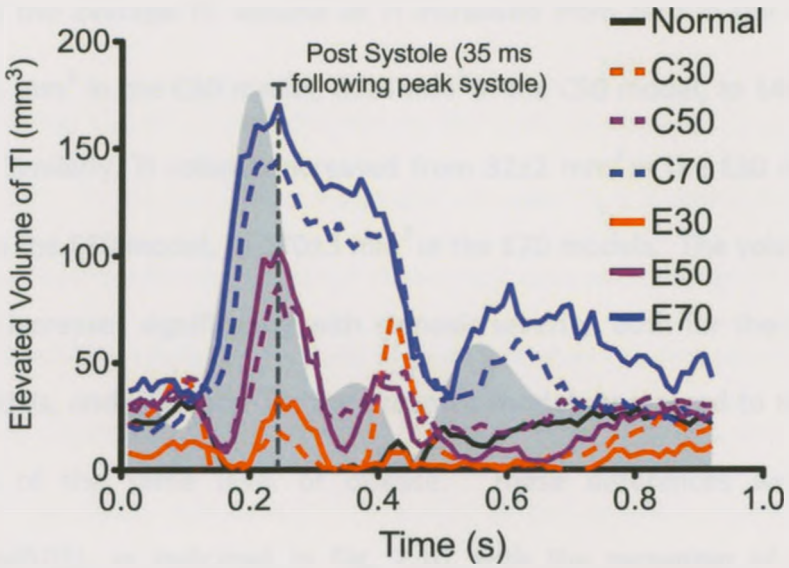

Figure 2.9: Volume of elevated TI in the ICA exceeding a threshold of 10 cm s^{-1} as a function of the cardiac cycle. The grey shaded region in the background, for reference purposes, is the pump flow waveform. The local maximum volume of elevated TI occurs following peak systole, with all maxima occurring at approximately 35 ms after peak systole, as indicated by the dashed, vertical line.

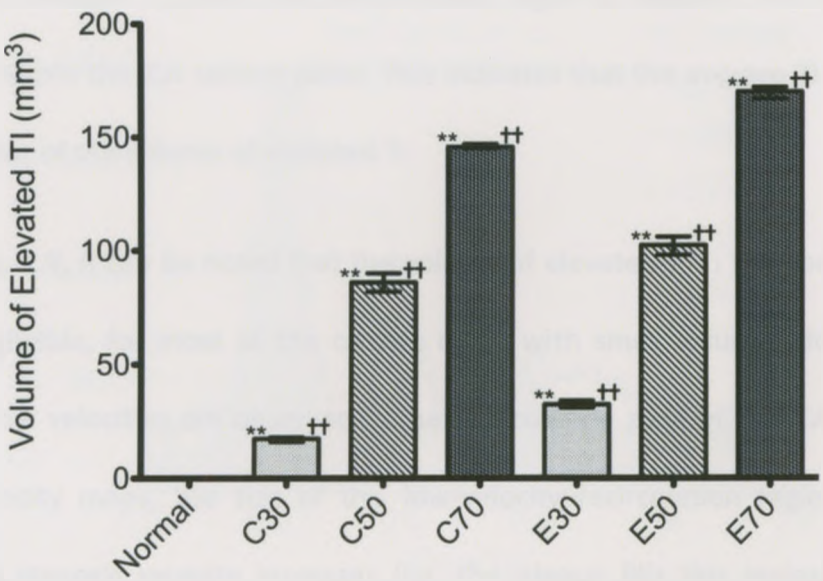

Figure 2.10: Maximum volume of elevated TI (exceeding a threshold of 10 cm s^{-1}) at the time of maximal volume. Statistical significance is indicated on the left side of the bars as an asterisks (*) for significance in difference between model eccentricity, while a cross (†) shown on the right of the bars show significance in the difference between the model indicated and the next less stenosed model of the same eccentricity. Here, differences were statistically significant at a level of $p<0.01$ based on a two-way ANOVA and Bonferroni post-hoc test.

Similar to the average TI, volume of TI increased from zero in the normal model, through 17±1 mm^3 in the C30 model, 86±4 mm^3 in the C50 model, to 146±1 mm^3 in the C70 model. Similarly, TI volume increased from 32±2 mm^3 in the E30 model, through 102±4 mm^3 in the E50 model, to 170±3 mm^3 in the E70 models. The volume of elevated TI in the ICA increases significantly with stenosis severity, both for the concentric and eccentric models, and is greater for the eccentric models compared to their concentric counterparts of the same level of disease. These differences were statistically significant ($p<0.01$), as indicated in Fig. 2.10, with the exception of the difference between the normal model and the concentric 30% model ($p>0.05$).

Additionally, a Pearson-r correlation coefficient of 0.96 indicates a strong correlation between the average TI across the central-plane region of interest and the volume of elevated TI within the ICA central-plane. This indicates that the average TI may be used as an indicator of the volume of elevated TI.

From Fig. 2.9, it can be noted that the volume of elevated TI in the normal model is zero, or negligible, for most of the cardiac cycle, with small volumes during diastole when very low velocities are observed in the recirculation zone of the ICA bulb. From the 2-D velocity maps, the size of this low-velocity recirculation region is seen to decrease as stenosis severity increases (i.e. the plaque fills this region), leading to recirculation regions of more complex and disturbed flow further downstream.

2.3.4 Cumulative TI

The cumulative TI, which was defined as the sum of elevated TI over the ICA, is shown in Fig. 2.11. This is the spatial integral of elevated TI; it is similar to the volume of elevated TI, but emphasizes the values of TI and thus accounts for high TI values. To this end, it is expected that similar trends will be seen between the two parameters. That is, increasing stenosis severity results in increasing cumulative TI, as was seen in Fig. 2.9 for volume of TI. Similarly, cumulative TI is higher in the eccentric models than in the concentric models of the same stenosis severity for time points near peak systole. During late diastole, this trend does not hold, but a similar trend to that seen during diastole in the volume of elevated TI is exhibited.

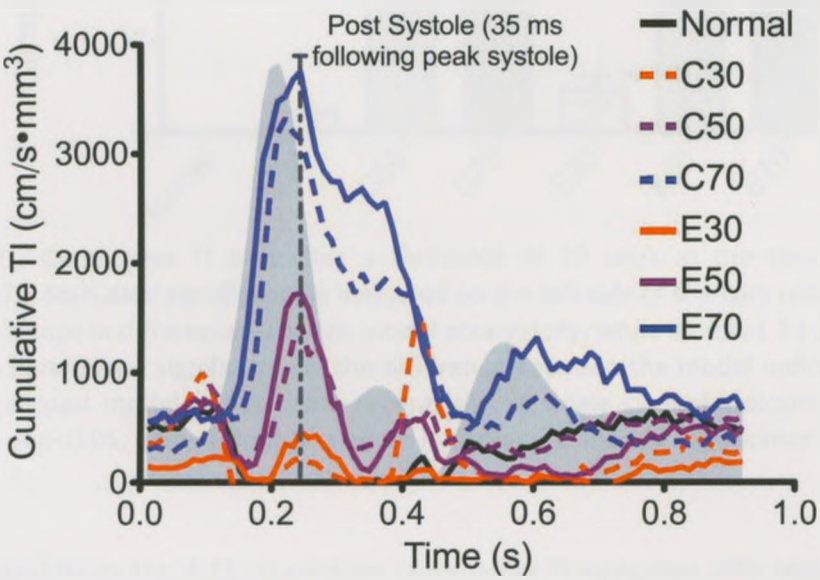

Figure 2.11: Cumulative TI exceeding a threshold of 10 cm s^{-1} as a function of the cardiac cycle. The grey shaded region in the background is the pump flow waveform, which has been added for reference purposes. The maximum cumulative TI occurs at times following peak systole, with the majority occurring at approximately 35 ms after peak systole, indicated by the dashed, vertical line.

The maximum cumulative TI is shown in Fig. 2.12. This is a single time point snap shot of cumulative TI taken at the time point of for which cumulative TI is maximal. This time point was not assumed to correspond between models, or with the time points of the average TI in the ROI or of the volume of elevated TI; however, the time point of maximal cumulative TI happened to be the same as the time point of the maximum volume of TI in the ICA.

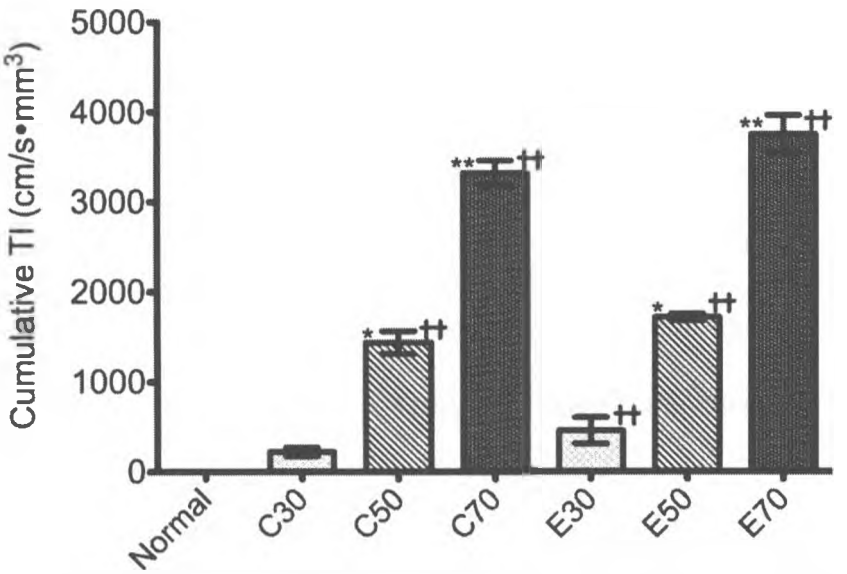

Figure 2.12: Cumulative TI exceeding a threshold of 10 cm/s at the time of maximal cumulative TI. Statistical significance is indicated on the left side of the bars with an asterisks (*) for significance in difference between model eccentricity, while a cross (†) shown on the right of the bars shows significance in the difference between the model indicated and the next less stenosed model of the same eccentricity. A single symbol indicates a statistical significance of $p<0.05$, while a double symbols indicates a statistical significance of $p<0.01$.

As expected from Fig. 2.11, maximum cumulative TI increases with stenosis severity, with eccentric models exceeding their concentric counterparts. Maximum cumulative TI increases from zero in the normal model, through 220±50 cm/s·mm^3 in the C30 model and 1440±130 cm/s·mm^3 in the C50 model to 3330±140 cm/s·mm^3 in the C70 model.

Similarly, maximum cumulative TI increases from 460±150 cm/s·mm^3 in the E30 model, through 1720±40 cm/s·mm^3 in the E50 model to 3750±210 cm/s·mm^3 in the E70 model. These trends are statistically significant, with significance levels given in Fig. 2.12, except for the difference between the concentric and eccentric 30% models. This is likely due to the overestimation of the error in the eccentric 30% model. Maximum cumulative TI was found to be correlated to both average TI in the ROI and volume of TI in the ICA exceeding the threshold with Pearson-r correlation coefficients of 0.9562 and 0.9843 respectively.

The cumulative TI accumulated over time (in the ICA) is shown in Fig. 2.13. Integrated cumulative TI increases from 291±26 cm/s·mm^3·s in the normal model, through 251±6 cm/s·mm^3·s in the C30 model and 491±9 cm/s·mm^3·s in the C50 model to 913±8 cm/s·mm^3·s in the C70 model. Similarly, integrated cumulative TI increases from 102±3 cm/s·mm^3·s in the E30 model through 414±5 cm/s·mm^3·s in the E50 model to 1261±13 cm/s·mm^3·s in the E70 model. Integrated cumulative TI increases with stenosis severity, except when comparing the normal model to the 30% models.

Integrated cumulative TI is also statistically significantly different between the eccentric models and their concentric counterparts for all stenosis severities, with statistical significance levels given in Fig. 2.13. However, for the 30% and 50% models, this difference is actually a decrease in integrated cumulative TI for the eccentric models over their concentric counterparts. It has previously been shown that time points near peak systole result in the formation of the high velocity jet which leads to the activation

of platelets (Einav and Bluestein, 2004); this time frame is also important for flow disturbances to yield optimal sites for thrombus formation. However, the long duration of non-insignificant cumulative TI during diastole contributes largely to the integrated cumulative TI, overshadowing the effects seen at time points of maximum volume of elevated TI and maximum cumulative TI.

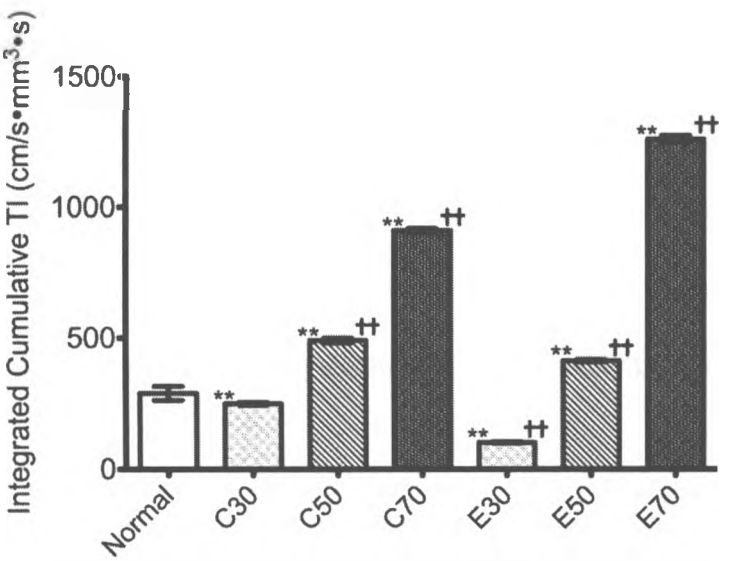

Figure 2.13: Cumulative TI exceeding a threshold of 10 cm s^{-1} integrated over all time in the cardiac cycle. Statistical significance is indicated on the left side of the bars as an asterisks (*) for significance in difference between model eccentricity, while a cross (†) shown on the right of the bars show significance in the difference between the model indicated and the next less stenosed model of the same eccentricity. Here, differences were statistically significant at a level of $p<0.01$ based on a two-way ANOVA and Bonferroni.

2.4 Discussion

While a threshold of 10 cm/s was selected for this study, it is important to note that the volume of elevated TI in the ICA was relatively insensitive to the threshold value over a range of 5-20 cm/s. While the total volume exceeding the threshold in each model changed with the threshold used (i.e. the volumes decreased for a higher

threshold and vice-versa), the shape of the curves was quite consistent between different thresholds. Also, near peak systole, the volume of TI exceeding the threshold in the normal model remained negligible until the threshold was dropped to below about 5 cm/s. This corresponds to the same threshold at which the volume in all models in diastole became significantly close to that seen during systole, suggesting 5 cm/s is the baseline level of system noise and random, cycle-to-cycle fluctuations for the flow system. Finally, for thresholds above about 20 cm/s, the volumes exceeding the threshold in diastole tended to be quite low, but those seen in the 30% models during systole were decreased to zero, and the volumes in the 50% models were nearing negligible, suggesting that the threshold was no longer able to distinguish between models, and may have been eliminating significant and possibly problematic regions of turbulence.

It was shown above that the average TI in the ROI, the volume of elevated TI in the ICA, and the cumulative TI over time and space all increase with stenosis severity. These trends were all statistically significant, as was shown in Fig. 2.7, Fig. 2.9, and Fig. 2.11. However, this increasing trend occurs more rapidly in the eccentric models. Because thrombus formation has been directly and indirectly linked to turbulence (Smith et al, 1972; Stein and Sabbah, 1974; Bluestein et al, 2000), it would be expected that increased turbulence would be correlated with stroke risk. Thus, plaque eccentricity, which affects the turbulence levels downstream of arterial stenoses, may be a potential risk consideration for the future. This assertion is supported by findings seen in Wong et

al (2009) in which the incidence of an ulceration in a plaque increases the TI significantly.

While for the 30% and 50% stenosis severities, the average TI in the ROI is higher for the eccentric models than for their concentric counterparts, the ROI average is approximately equal for the 70% models within statistical uncertainties (23.5±1.6 and 23.4±1.9 cm/s for concentric and eccentric models respectively). Because the eccentric 70% model exceeds the concentric 70% model, as with the 30% and 50% models, for both maximal and cumulative area in the ICA, this would suggest that, while there is a difference in the flow characteristics distal to the stenosis due to plaque symmetry, there is a plateau at which point the effects of the flow disturbances due to the flow constriction overcome those due to the path of the unstable flow regions. This further supports the assertion that flow, more than just stenosis severity, should be a consideration in the assessment of stroke risk.

Wong et al (2009) previously showed that the maximum TI distal to a non-ulcerated 50% eccentric stenosed model was 18.5±0.4 cm/s. This value is slightly higher than that seen here (16.0±0.9 cm/s), due to the difference in the orientation and shape of the ROI. Furthermore, ulcerated models showed TI values in the range of 24 to 27 cm/s, values slightly higher than those seen in this study in the 70% models. Given the increase in TI seen in the comparable models, this may suggest that a 60% model (eccentric or concentric) would have similar downstream flow disturbances as seen in a 50% eccentric model with ulcerations.

Thorne et al (2010) looked at the average TI (using a slightly different method, but with comparable values) in patients as it relates to stenosis severity clinically. In this study, it was found that the average TI over 25 s of cardiac data at the site of maximal turbulence increased with stenosis severity as classified using NASCET standards (NASCET Steering Committee, 1991). This trend corresponds well to the trends seen in this study, in which cumulative TI over area and time increases with stenosis severity. Since Thorne did not consider the differences between eccentricities *in vivo*, these differences are not relevant for comparison.

One of the major limitations of this study was the use of the Teflon phantoms. Teflon is a very rigid material, so the compliance normally seen in the vasculature was not present; however this was a comparison study, so the trend between the different models was more important than the exact values seen in each model. Also, because of the high attenuation due to Teflon, there was significant signal loss, especially at the walls of the vessel. This signal loss was made that much worse because of the acoustic impedance mismatch between the Teflon and the blood mimicking fluid, which caused large amounts of refraction inside the vessel. Because of these two effects, volumetric data could not be obtained in the vessel, and only central plane data was obtained. Data near the walls was still noisier than that located more centrally in the vessel, which is also true for clinical ultrasound exams, as DUS is known for its unreliability when wall motion is seen. Also, because of the reduced diameter in the ECA, the higher attenuation caused extra noise such that this data was ignored for analysis and only the more reliable ICA data was considered. This was a valid omission as this portion of the

bifurcation is not a likely site of plaque buildup, nor is it a susceptible site for stroke: clots resulting from the ECA travel into the face, not into the brain.

Another limitation of the study is that it is difficult to measure an area or volume clinically. The number of scan lines required for a volume (or even an area) of data is large, and with each scan line taking some time, the loss in temporal resolution would be a hindrance. Furthermore, it may require advancements in depth gating and signal processing before these calculations can be made in real time. The study does show valuable information that cannot otherwise be seen, however, and would not be able to be considered without a controlled *in vitro* system. The correlation between the cumulative data, volumetric data and ROI averages provides a strong case for the consideration of this method for clinical use.

With the use of current or advanced depth gating techniques, offline analysis could be used to clinically assess patients with respect to severity of carotid disease using the average TI in a region in the ICA distal to the bifurcation. Furthermore, a possible clinical trial could assess the risk of stroke based on the aforementioned technique. For ease of use, an *in vivo* module on a clinical ultrasound system that could provide color TI, similar to standard color Doppler images typically available on a clinical system (possibly using a method similar to that described by Thorne et al (2010)), while performing real-time analysis would be ideal for these applications.

2.5 Conclusion

An *in vitro* flow system has been used to measure turbulence intensity as a spectral parameter of Doppler ultrasound. It was found that, within the central plane of the ICA, the volume of elevated TI increases with stenosis severity from zero in the normal model to 146±1 and 170±3 mm^3 in both of the severely stenosed concentric and eccentric models, respectively. The maximum cumulative TI increased from zero in the normal model to 3330±140 and 3750±210 $cm/s \cdot mm^3$ in the severely stenosed models. The volume of elevated TI was correlated to maximum cumulative TI with a Pearson-r correlation coefficient of 0.98. The eccentric models were also found to have higher volumes than their concentric counterparts for all models. The average TI over a 25-mm^2 region 1.5 cm (~2 CCA diameters) distal to the carotid bifurcation was found to have trends correlated with the volume of elevated TI (Pearson-r statistic of 0.96) and with the maximum cumulative TI (Pearson-r statistic 0.96); it increased from 2.3±0.2 cm/s in the normal to 23.5±1.6 and 23.4±1.9 cm/s in the 70% stenosed models. This shows that, while volume of TI is an advanced indicator of stenosis severity, and may possibly be its own indicator of stroke risk, measuring the average TI in a region distal to the stenosis is a more feasible clinical indicator of the volume with much more potential for lasting impact in real world applications.

2.6 References

Barnes RW. Noninvasive diagnostic-assessment of peripheral vascular-disease. Circulation 1991; 83:20-27

Barnett HJM, Gunton RW, Eliasziw M, Fleming L, Sharpe B, Gates P, Meldrum H. Causes and severity of ischemic stroke in patients with internal carotid artery stenosis. JAMA 2000; 283:1429-1436

Barnett HJM, Taylor DW, Eliasziw M, Fox AJ, Ferguson GG, Haynes RB, Rankin RN, Clagett GP, Hachinski VC, Sackett DL, Thorpe KE, Meldrum HE, Spence JD. Benefit of carotid endarterectomy in patients with symptomatic moderate or severe stenosis. N Engl J Med 1998; 339:1415-1425

Bowman JN, Olin JW, Teodorescu VJ, Carroccio A, Ellozy SH, Marin ML, Faries PL. Carotid artery pseudo-occlusion: does end-diastolic velocity suggest need for treatment? Vasc Endovascular Surg 2009; 43: 374-378

Bluestein D, Rambod E, Gharib M. Vortex shedding as a mechanism for free emboli formation in mechanical heart valves. J Biomech Eng: Trans ASME 2000; 122: 125-134

Chambless LE, Heiss G, Folsom AR, Rosamond W, Szklo M, Sharrett AR, Clegg LX. Association of coronary heart disease incidence with carotid arterial wall thickness and major risk factors: the atherosclerosis risk in communities (ARIC) study, 1987-1993. Am J Epidemiol 1997; 146:483-494

Chow TW, Hellums JD, Thiagarajan P. Thrombin receptor activating peptide (SFLLRN) potentiates shear-induced platelet microvesiculation. J Lab Clin Med 2000; 135:66-72

Constantinides P. Cause of thrombosis in human atherosclerotic arteries. American J Cardiol 1990; 66:G37-G40

Cunningham KS, Gotlieb AI. The role of shear stress in the pathogenesis of atherosclerosis. Lab Invest 2005; 85:9-23

Dai S, Bancej C, Bienek A, Walsh P, Stewart P, Wielgosz A. Tracking heart disease and stroke in Canada 2009. Chronic Dis Can 2009; 29 (4): 192-193

Einav S, Bluestein D. *Dynamics of blood flow and platelet transport in pathological vessels*. In: Sideman S, Beyar eds. Cardiac Engineering: from Genes and Cells to Structure and Function. New York, NY: New York Academy of Sciences, 2004; vol. 1015 pp. 351-366

Ferguson GG, Eliasziw M, Barr HWK, Clagett GP, Barnes RW, Wallace MC, Taylor DW, Haynes RB, Finan JW, Hachinski VC, Barnett HJM. The North American Symptomatic

Carotid Endarterectomy Trial: surgical results in 1415 patients. Stroke 1999; 30:1751-1758

Ford MD, Alperin N, Lee SH, Holdsworth DW, Steinman DA. Characterization of volumetric flow rate waveforms in the normal internal carotid and vertebral arteries. Physiol Meas 2005: 26:477-488

Glantz SA. The Bonferroni *t* Test. In: Malley J, Lebowitz H, Davis K, eds. Primer of Biostatistics. 6th Ed. New York, NY: The McGraw Hill Medical Publication Division, 2005. pp. 98-100.

Heart and Stroke Foundation of Canada. Heart Disease and Stroke Statistics. 2011. http://www.heartandstroke.on.ca/site/c.pvI3IeNWJwE/b.3581729/k.359A/Statistics.htm

Hellums JD. 1993 Whitaker Lecture: Biorheology in thrombosis research. Ann Biomed Eng 1994; 22:445-455

Holdsworth DW, Rickey DW, Drangova M, Miller DJM, Fenster A. Computer-controlled positive displacement pump for physiological flow simulation. Med Biol Eng Comput 1991; 29:565-570.

Holdsworth DW, Norley CJD, Frayne R, Steinman DA, Rutt BK. Characterization of common carotid artery blood-flow waveforms in normal human subjects. Physiol Meas 1999; 20:219-240

Inzitari D, Eliasziw M, Gates P, Sharpe BL, Chan RKT, Meldrum HE, Barnett HJM. The causes and risk of stroke in patients with asymptomatic internal-carotid-artery stenosis. N Engl J Med 2000; 342:1693-1700

Jackson SP, Nesbitt WS, Westein E. Dynamics of platelet thrombus formation. J Thromb Haemos 2009; 7:17-20

Johnston KW, Baker WH, Burnham SJ, Hayes AC, Kupper CA, Poole MA. Quantitative analysis of continuous-wave Doppler spectral broadening for the diagnosis of carotid disease: Results of a multicenter study. J Vasc Surg 1986; 4:493-504

Ku DN. Blood flow in arteries. Annu Rev Fluid Mech 1997; 29:399-434

Mays BW, Towne JB, Seabrooke GR, Cambria RA, Jean-Claude J. Intraoperative carotid evaluation. Arch Surg 2000; 135:525-529

McDonald JH. *Handbook of Biological Statistics (2nd Ed)*. Baltimore, MD: Sparkyhouse Publishing, 2009. pp.182-190

North American Symptomatic Carotid Endarterectomy Trial Steering Committee. North American Symptomatic Carotid Endarterectomy Trial: methods, patients, characteristics and progress. Stroke 1991; 22:771-720

Perrin G, Goutelle A, Pierluca P, Chacornac R, Allegre GE. Reliability of Doppler ultrasound diagnosis in carotid-artery stenosis. Neurochirurgie 1977; 23:215-225

Poepping TL, Nikolov HN, Rankin RN, Lee M, Holdsworth DW. An in vitro system for Doppler ultrasound flow studies in the stenosed carotid artery bifurcation. Ultrasound Med Biol 2002; 28:495-506

Public Health Agency of Canada. *Tracking Heart Disease and Stroke in Canada*. 2009.

Ramnarine KV, Nassiri DK, Hoskins PR, Lubbers J. Validation of a new blood-mimicking fluid for use in Doppler flow test objects. Ultrasound Med Biol 1998; 24:451-459

Raz S, Einav S, Alemu Y, Bluestein D. Prediction of flow induced platelet activation – comparison to numerical predictions. Ann Biomed Eng 2007; 35:493-504

Rittgers SE, Thornhill BM, Barnes RW. Quantitative analysis of carotid artery Doppler spectral waveforms: diagnostic value of parameters. Ultrasound Med Biol 1983; 9:255-264

Smith RF, Rutt BK, Fox AJ, Rankin RN. Geometric characterization of stenosed human carotid arteries. Acad Rad 1996; 3:898-911

Smith RL, Stein PD, Coalson J, Blick EF. Thrombus production by turbulence. Am Physiol Soc 1972; 32:261-264

Spence JD. Asymptomatic Carotid Stenosis: Mainly a Medical Condition. Vascular 2010; 18:123-126

Srinivasan J, Mayberg MR, Weiss DG, Eskridge J. Duplex accuracy compared with angiography in the veterans affairs cooperative studies trial for symptomatic carotid stenosis. Neurosurgery 1995; 36:648-653

Statistics Canada. *CANSIM Table 102-0529: Deaths, by cause, Chapter IX: Diseases of the circulatory system (I00 to I99), age group and sex, Canada, annual (number), 2000 to 2006*. Released May 4, 2010

Stein PD, Sabbah HN. Measured turbulence and its effect on thrombus formation. Circ Res 1974; 35:608-614

Thorne ML, Poepping TL, Nikolov HN, Rankin RN, Steinman DA, Holdsworth DW. In vitro Doppler ultrasound investigation of turbulence intensity in pulsatile flow with simulated cardiac variability. Ultrasound Med Biol 2009; 35:120-128

Thorne ML, Poepping TL, Rankin RN, Steinman DA, Holdsworth DW. Use of an ultrasound blood-mimicking fluid for Doppler investigations of turbulence in vitro. Ultrasound Med Biol 2008; 34:1163-1173

Thorne ML, Rankin RN, Steinman DA, Holdsworth DW. In Vivo Doppler Ultrasound Quantification Of Turbulence Intensity Using A High-Pass Frequency Filter Method. Ultrasound Med Biol 2010; 36:761-777

Tola M, Yurdakul M. Effect of Doppler angle in diagnosis of internal carotid artery stenosis. J Ultrasound Med 2006; 25:1187-1192

Van Popele NM, Grobbee DE, Bots ML, Asmar R, Topouchian J, Reneman RS, Hoeks APG, van der Kuip DAM, Hofman A, Witteman JCM. Association between arterial stiffness and atherosclerosis: the Rotterdam study. Stroke 2001; 32:454-460

Warlow CP. Symptomatic patients – the European carotid surgery trial (ECST). J Mal Vasc 1993; 18:198-201

Wong EY, Nikolov HN, Thorne ML, Poepping TL, Rankin RN, Holdsworth DW. Clinical Doppler ultrasound for the assessment of plaque ulceration in the stenosed carotid bifurcation by detection of distal turbulence intensity: a matched model study. Eur Radiol 2009; 19:2739-2749

Wong EY, Thorne ML, Nikolov HN, Poepping TL, Holdsworth DW. Doppler ultrasound compatible plastic material for use in rigid flow models. Ultrasound Med Biol 2008; 34:1846-1856

Chapter 3 Summary, Conclusions and Future Work

3.1 Summary and Conclusions

3.1.1 Summary

Chapter 2 described an *in vitro* flow experiment used to assess the flow disturbances downstream of the carotid stenosis in seven flow models. Turbulence intensity was measured in the central plane of seven models and assessed in terms of volumetric extent and regional average. The cumulative TI was also determined. These were all considered as a function of the cardiac cycle and at a single time for which the parameter exhibited a local maximum near peak systole for each model. Cumulative TI was also integrated over time in a manner analogous to the *level of activation parameter* (summation over the path length of the product of shear stress and exposure time) presented by Bluestein et al (1997).

The volume of elevated TI was measured as the number of voxels in the central plane of the internal carotid artery (ICA) exceeding a threshold of 10 $cm \cdot s^{-1}$, an upper limit estimate of clinically non-significant TI accounting for random noise, cycle-to-cycle velocity variability and fluctuations due to wall filter errors. The volume of TI increased with stenosis severity from zero in the non-stenosed, disease-free (normal) model to 146 ± 1 and 170 ± 3 mm^3 in the concentric and eccentric severely stenosed models, respectively. These increases were between 70% and 400% over the model of the next lowest stenosis severity and the same eccentricity. There was a 15% (E70 vs. C70) to

100% (E30 vs. C30) increase in TI volume when considering the eccentric models over the concentric models.

Cumulative TI was defined to be the spatial integral of elevated TI values (those values exceeding the same 10 $cm \cdot s^{-1}$ threshold) over the ICA. Not surprisingly, this parameter was highly correlated to the volume of elevated TI, with a Pearson-r coefficient of 0.9843. This is expected since it is merely another measure of volume, using a weighting of TI values to emphasize those points with more elevated TI, which are already accounted for in the binary sum of TI volume. Cumulative TI increased from zero in the normal model to 3320 ± 140 and 3750 ± 210 $cm/s \cdot mm^3$ in the concentric and eccentric severely stenosed models, respectively. These increases were between two- and six-fold between models of consecutive stenosis grades of the same symmetry. Cumulative TI also increased by between 10% (E70 vs. C70) and 100% (E30 vs. C30) for eccentric models over concentric models of the same stenosis severity.

The average TI in the region of interest (ROI) was defined as the average value of TI over a square ROI with area 25 mm^2 (5 mm across), 1.5 cm (approximately 2 common carotid artery (CCA) diameters) distal to the carotid bifurcation. The ROI averaged TI increased with stenosis severity from 2.3 ± 0.2 $cm \cdot s^{-1}$ in the normal model, to 23.5 ± 1.6 and 23.4 ± 1.9 $cm \cdot s^{-1}$ in the concentric and eccentric severely stenosed models, respectively. The increase in ROI averaged TI was between 40% and 400% for consecutive increases in stenosis severity. While there was no difference between the concentric and eccentric models with severe stenosis, the mildly and moderately

stenosed models had ROI averaged TI values that were 100% and 50% higher, respectively, in the eccentric model than the corresponding concentric model. These trends are similar to those seen in the volume of TI and the cumulative TI, both having a Pearson-r correlation coefficient of 0.96.

3.1.2 Conclusion

It has been shown that TI increases with stenosis severity, both in magnitude and volume in the ICA. This increase in TI is accentuated in phantoms modeling asymmetric plaque buildup at the site of the stenosis. While the increased volume of elevated TI may be indicative of higher platelet activation and formation of larger thrombi, due to longer exposure times (Bluestein et al, 2002; Nygaard et al, 1992), volumetric measurements are difficult and impractical. As such, the TI averaged over a small ROI is considered as a more clinically feasible measurement. The strong correlation between ROI average TI and both volume and cumulative TI suggests that the average TI in the ROI may be used as a surrogate measure for the other two parameters.

3.2 Future Work

3.2.1 Validation of Data

Because of the errors associated with Doppler ultrasound (DUS), especially those associated with angle dependence (Tola and Yurdakul, 2006), validation of the experimental data against a robust, vector-capable system would be ideal. Computational fluid dynamics (CFD) offers one such method for this. CFD is a high

resolution method for finding numerical solutions to fluid dynamics equations in models of flow systems (Wesseling, 2009). Some work has been done previously on similar flow models, but comparison to the full set of exact flow models would be beneficial (Wong et al, 2008; Hoskins, 2008).

Another, less time consuming method of comparison is particle imaging velocimetry (PIV). In this method, transparent models are used with a transparent, refractive index matched fluid (Yousif et al, 2011) and cross correlation methods are used to determine the flow velocity between two consecutive images of the flow channel (Raffel et al, 2007). Stereoscopic PIV provides a third vector component to these measurements (Arroyo and Greated, 1991). This method would eliminate errors due to measuring velocities in turbulent areas, which are problematic in CFD.

3.2.2 Clinical Experimentation

The present work determined that the average TI in a ROI distal to the carotid bifurcation correlates well to cumulative and volumetric measurements of TI, this parameter could be used in a clinical trial to assess a possible correlation between TI and stroke risk in less stenosed patients. Based on the guidelines derived by the North American Symptomatic Carotid Endarterectomy Trials (NASCET) (Barnett et al, 2000), all symptomatic patients with severely stenosed carotid arteries are now immediately scheduled for carotid endarterectomy (CE). Because of this decision, these patients are no longer available for further study; it would thus be required that any further clinical trials investigating stroke risk be performed on patients with <70% stenosis severity.

A clinical DUS system that can perform real-time TI measurements would be beneficial for clinical assessment of TI in patients; however, for early studies, offline post-analysis would be feasible. For either of these methods, an alternative measure of TI would need to be implemented which accounts for the cycle-to-cycle variability in the flow rate and cycle length (Holdsworth et al, 1999). This method was presented by Thorne et al (2010) and shown to give a similar measure of TI.

A depth-gating technique would also need to be implemented, with several successive scan lines acquired in order to obtain data from multiple sites in the region of the bifurcation. Depth-gating is a technique which segments the received data into multiple sample volumes (gates) based on the time-of-flight concept of reflections from deeper parts of the vessel taking longer to return to the transducer. Enlarging the sample size is ineffective as it causes the small scale fluctuations of the turbulence to be averaged out within the acquisition volume.

3.2.3 Application to Other Fluid Dynamic Systems

The methodology in this work has been applied to a family of carotid bifurcation models simulating concentric and eccentric plaque buildup of the ICA. However, this same methodology could be used to investigate TI, and thus downstream flow disturbances, in any flow system. Further investigation could be made into the downstream turbulence changes resulting from varying arterial stiffness, both in the model itself and in the downstream compliance, to model healthy, aging and stiffened diabetic patient arteries (van Popele et al, 2001; Parikh et al, 2000). Patient specific

geometries could also be studied; however, these models would be time consuming and difficult to fabricate, and thus would not be as practical as clinical trials with a non-invasive measure such as DUS. Studies could also be performed on models of stenosed aortic arteries, where flow disturbances are known to be high in patients with aortic stenoses and mechanical heart valves (Stein and Sabbah, 1976; Nygaard et al, 1992).

Finally, it could also be possible to apply this methodology for non-destructive flow testing in non-medical applications. Many applications, such as aerodynamics (Hsiao et al, 2011) and supercritical water hydrothermal reactors (Sierra-Pallares et al, 2011), rely on elevated levels of turbulence for their intrinsic fluid mechanical properties (lower pressures, efficient mixing, etc.). Others, such as oceanographic studies (Dolgopolov and Isupova, 2010; Scotti, 2010), simply investigate this turbulence to infer some information about the size of eddy currents or vortices. The above described methods could be used in a number of industrial and research applications to take measures of turbulence using DUS.

3.3 References

Arroyo MP, Greated CA. Stereoscopic particle image velocimetry. Meas Sci Technol 1991; 2: 1181-1186

Barnett HJM, Gunton RW, Eliasziw M, Fleming L, Sharpe B, Gates P, Meldrum H. Causes and severity of ischemic stroke in patients with internal carotid artery stenosis. JAMA 2000; 283:1429-1436

Bluestein D, Li YM, Krukenkamp IB. Free emboli formation in the wake of bi-leaflet mechanical heart valves and the effects of implantation techniques. J Biomech. 2002; 35: 1533-1540

Bluestein D, Niu L, Schoephoerster RT, Dewanjee MK. Fluid mechanics of arterial stenosis: relationship to the development of mural thrombus. Ann Biomed Eng 1997; 25: 344-356

Dolgopolov EN, Isupova MV. Classification of estuaries by hydrodynamic process. Water Resour 2010; 37: 268-284

Holdsworth DW, Norley CJ, Frayne R, Steinman DA, Rutt BK. Characterization of common carotid artery blood-flow waveforms in normal human subjects. Physiol Meas 1999; 20: 219-240

Hoskins PR. Simulation and validation of arterial ultrasound imaging and blood flow. Ultrasound Med Biol 2008; 34: 693-717

Hsiao FB, Lim YC, Huang JM. On evolution of flow structure and vortex dynamics for right-angle and sharp-edged orifice plane jet. Trans Jpn Soc Aeronaut Space Sci 2011; 53: 296-306

Nygaard H, Giersiepen M, Hasenkam JM, Reul H, Paulsen PK, Rovsing PE, Westphal D. 2-Dimensional color-mapping of turbulent shear-stress distribution downstream of 2 aortic bioprosthetic valves in vitro. J Biomech. 1992; 25: 429-440

Parikh A, Sochett EB, McCrindle BW, Dipchand A, Daneman A, Daneman D. Carotid artery distensibility and cardiac function in adolescents with type 1 diabetes. J Pediatr 2000; 137; 465-469

Raffel M, Willert CE, Wereley ST, Kompenhans J. *Particle Image Velocimetry: A Practical Guide*. Berlin, Germany: Springer. 2007

Scotti A. Large eddy simulation in the ocean. Int J Comput Fluid Dyn. 2010; 24: 393-406

Sierra-Palleras J, Marchisio DL, Alsonso E, Para-Santos MT, Castro F, Cocero MJ. Quantification of mixing efficiency in turbulent supercritical water hydrothermal reactors. Chem Eng Sci 2011; 6: 1576-1589

Stein PD, Sabbah HN. Turbulent blood flow in the ascending aorta of humans with normal and diseased aortic valves. Circ Res 1976; 39: 58–65.

Tola M, Yurdakul M. Effect of Doppler angle in diagnosis of internal carotid artery stenosis. J Ultrasound Med 2006; 25:1187-1192

Thorne ML, Rankin RN, Steinman DA, Holdsworth DW. In vivo Doppler ultrasound quantification of turbulence intensity using a high-pass frequency filter method. Ultrasound Med Biol 2010; 36: 761-771

Van Popele NM, Grobbee DE, Bots ML, Asmar R, Topouchian J, Reneman RS, Hoeks APG, van der Kuip DAM, Hofman A, Witteman JCM. Association between arterial stiffness and atherosclerosis: the Rotterdam Study. Stroke 2001; 32: 454-460

Wesseling P. *The basic equations of fluid dynamics*. In: Bank R, Graham RL, Stoer J, Varga R, Yserentant H, eds. Principles of Computational Fluid Dynamics. Berlin, Germany: Springer, 2009. pp. 1-52

Wong EY, Milner JS, Thorne ML, Nikolov HN, Steinman DA, Rankin RN, Poepping TL, Holdsworth DW. *Doppler ultrasound and numerical analysis for the assessment of hemodynamic disturbances in ulcerated carotid arteries*. Proc IEEE Ultrason Symp. Beijing, Peoples Republic of China, Nov 2008. pp. 1603-1606

Yousif MY, Holdsworth DW, Poepping TL. A blood-mimicking fluid for particle imaging velocimetry with silicone vascular models. Exp Fluids 2001; 50: 769-774

Appendix A Detailed Methodology of Experimentation

A.I *In Vitro* Flow Facility

A.I.I Flow

For collection of the central plane data in the seven anthropomorphic phantoms, an *in vitro* flow facility was utilized (Poepping et al, 2002). A commercially available, positive-displacement flow pump (Compuflow 1000, Shelley Medical, Toronto, ON, Can) provides fluid flow for perfusion to the hemodynamic components of the system (Holdsworth et al, 1991). This flow is physiologically realistic for the carotid artery, based on flow studies performed by Holdsworth et al (1999).

A Doppler ultrasound (DUS) compatible blood mimicking fluid (BMF), as described in Poepping et al (2002) is used in the flow loop for the flow experiments. This fluid consists mainly of distilled water, glycerol and dextran to achieve the desired viscosity (4.1±0.1 mPa·s), density (1037±2 kg/m^3) and speed of sound (1547 cm/s) to approximate blood. A preservative, small nylon scatterers, and a surfactant are also added in small quantities to increase the shelf-life of the BMF, create an appropriate ultrasound (US) backscatter, and enable dispersion of the scattering particles, respectively.

Flow first passes through the anthropomorphic phantom, then travels through small diameter intravenous (IV) tubing which provides resistance to mimic the physiological flow resistance seen *in vivo* (Bogren et al, 1994; Schoning et al, 1994). This flow

resistance also determines the flow division between the internal carotid artery (ICA) and external carotid artery (ECA) of 65% and 35% respectively, which is physiologically realistic.

A.I.II Phantoms

A collection of seven phantoms was created and used for this experiment, based on geometries described by Smith et al (1996). A normal model, simulating a carotid artery with no arterial disease, served as the baseline for all other models. The other six models can be divided into two categories: concentric models and eccentric models. The concentric models simulate a rotationally symmetric build-up of plaque in the ICA, while the eccentric models simulate an asymmetric build-up of plaque on the outer (lateral) wall of the ICA, opposite to the bifurcation apex. Each category also models a progression of simulated plaque from mild stenosis severity (30% by North American Symptomatic Carotid Endarterectomy Trials (NASCET) criteria, through moderate (50%) to severe (70%) stenosis severity (NASCET Steering Committee, 1991).

The phantoms used in this experiment are fabricated using a technique described by Wong et al (2008). Briefly, in this method, the desired geometry of the carotid artery is split into two symmetric halves through the center of both the ICA and the ECA. The parametric surfaces of these two mirrored half-arteries are then programmed into a CAD software package (MasterCam, CNC Software Inc., Tolland, CT, USA). Finally, two 5-mm thick sheets of Teflon® are individually machined using a numerically-controlled router (Millenium Series, AXYZ Automotion Inc., Burlington, ON, Canada). Four

centering pinholes are also machined into each half of the phantom for alignment and assembly.

Once the phantom halves are machined, they must be assembled. Using 6.4-mm diameter dowels in the centering holes, the phantom halves are assembled and sealed using a silicon sealant. Threaded holes are then drilled into the ends of the phantom at the ends of the common carotid artery (CCA), ICA and ECA and flow connectors and threaded into the holes and sealed.

A.I.III Doppler Ultrasound System

The flow facility uses a commercially available, clinical DUS system which is connected to a traditional vascular US transducer probe with a 4 MHz central pulse frequency (HDI 5000, Philips-ATL, Oceanside, CA, USA). The transducer is secured to the control arm of a three-axis translational stage and motion of this stage is computer controlled.

A.II Phantom and Transducer Alignment

A.II.I Phantom Alignment in the Water Bath

Once the silicone is set in the phantom, it is connected into the flow loop in the empty water bath container. The pump is turned on to a slow, steady flow rate, and the phantom is checked for leaks. If the phantom is leaking, it is removed and resealed. If there are no leaks, the flow rate is increased to a maximum of 10 mL/s. The distal

portion of the tubing is elevated so that any trapped air bubbles proceed out of the phantom and through the remainder of the tubing and back into the pump. Finally, a level is used to ensure that the phantom is level in all directions within the experimental setup.

The water bath is then filled with water, a very small amount of soap is added to help release any trapped dissolved gasses, and any air bubbles are dislodged from the underside of the phantom and its connectors. An offset block is placed under the phantom, to reduce reflections. Because the water bath material has a high impedance mismatch to water, there will be large reflections due to this interface. These reflections show up in the center of the phantom, within the vessel, so a block of attenuating material, with similar acoustic impedance to water (in this case an agar-like gel block) will absorb some of the energy of the reflected beam, lessening its effect, and shifting its position.

A.II.II Transducer Alignment in the Phantom Flow Channel

Once the phantom is set up and aligned in the water bath, the transducer must be aligned to collect data from the correct position in the phantom. To do this, steady flow is maintained, and the US transducer is shifted into the approximate position of the center of the CCA, approximately halfway between the flow connectors and the branching point of the bifurcation, using the computer controlled translational stage. The transducer is then rotated so that the DUS sample volume aligns with the upper wall of the flow channel. The sample volume may have to be moved to achieve this. A

60° Doppler angle is used for consistency, and the transducer is rotated until this angle matches the wall of the vessel. Then the sample volume is moved to the center of the screen, and shifted until it is at a depth of 2.3 cm, the second focal depth of the transducer. The smallest possible wall filter setting (approximately 50 Hz) was also applied at this time, in case adjusting the wall filter changes the position of the center of the sample volume once it is aligned.

Next, the transducer is shifted up or down until the sample volume is seen to be at the approximate vertical center of the flow channel. Doppler data are collected on the US machine and the transducer is shifted an identical distance (usually 3 mm) both left and right of the assumed center position and compared to each other; if the center is chosen correctly, the symmetric velocity profile ensures that the shifted positions will measure the same velocities. The measured velocity spectra are narrow in the CCA, so the comparison between points is easily made.

Because of the high velocity gradient near the walls, small errors in the position will be observed as large errors in the velocity, making it easy to determine if the central position has been incorrectly chosen. If one of the off-center velocities is higher than the other, the actual center of the vessel is not aligned with the assumed center of the vessel. The assumed vessel center must be shifted slightly towards the higher velocity side to compensate for this. Figure A.1 shows a schematic of this for parabolic, well developed flow. This process is repeated until the velocity profiles on either side of the central position are identical.

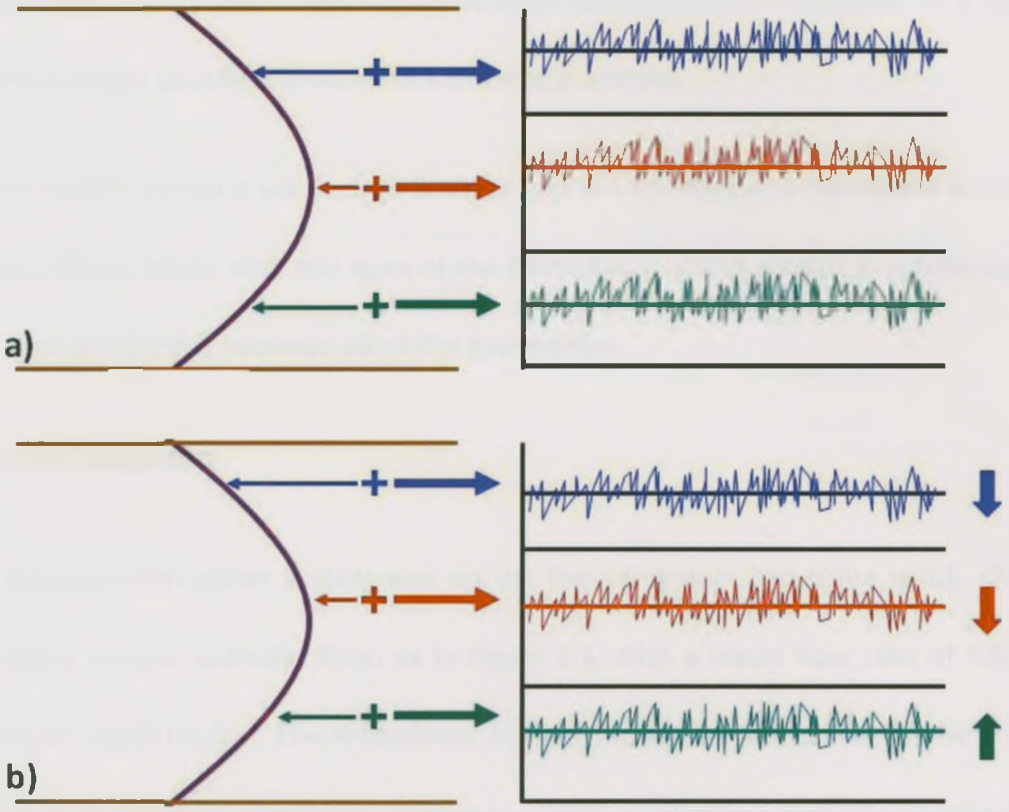

Figure A.1: A schematic of the centering procedure for alignment of the transducer at the center of the vessel, as shown for a horizontal plane through the center of the CCA with steady flow. In a), the assumed center (red cross) is at the center of the vessel, so that the mean velocity on either side of the vessel (green and blue crosses) have the same magnitude, shown to the right. In b), the assumed center is slightly above (in the image) the actual center. Because of this, the mean velocity in both the center and the above shifted positions (blue) are lower their expected values, and the below shifted position (green) is higher. The mean velocity shown in green is also higher than the mean velocity shown in blue when the central position is above the actual center, so the center must be shifted downwards, towards the higher velocity profile.

Once the horizontal center is found, the vertical center of the CCA must be located. A similar process is used as before, shifting the transducer up and down this time from the expected center of the vessel. However, a smaller shift must be used because the attenuation causes the received signal to have a lower amplitude, and thus a decreased

brightness, resulting in a loss in the higher velocity components of the signal. A 2 mm offset from center is usually sufficient for centering purposes.

Finally, the US system is set back to B-mode and the transducer is translated so that the sample volume aligns with the apex of the bifurcation, which is used as a landmark for consistent positioning between all of the geometries.

A.III Data Collection

Once the data acquisition system was set up, the US system had to be setup. The pump is set to cardiac pulsatile flow, as in figure 2.1, with a mean flow rate of 6.000 mL/s (peak of 23.46 mL/s). The transducer is then moved to the center of the high velocity jet and the pulse repetition frequency (PRF) is adjusted until the maximum velocity is below the maximum readable velocity by the US system. This required a PRF between 10 000 Hz (normal and 30% stenosed models) and 16667 Hz (70% models) corresponding to 1 -1.75 m/s respectively.

A sample data point is collected at this point and the audio file is examined to ensure there is no clipping in the spectra. Clipping is seen as flat spots in the otherwise rounded sinusoidal-like raw data signifying that the amplitude of the signal is too high and the gain must be decreased. Sample data is also collected in the fluctuating recirculation zone downstream of the jet (where velocity spectra tend to be broadest) and in the center of the CCA (where lower attenuation facilitates a wider spectrum and higher velocity components).

If the gain is found to be appropriately set in all of the sample data points, the data collection can begin. All of the parameters of the acquisition are recorded, the coordinate file delineating acquisition sites in the central plane is loaded, and the automatic acquisition software is started. A standard acquisition usually takes approximately nine hours to complete.

A.IV References

Bogren HG, Buonocore MH, Gu WZ. Carotid and Vertebral artery blood-flow in left-handed and right-handed healthy-subjects measured with MR velocity mapping. J Magn Reson Imaging. 1994; 4: 37-42

Holdsworth DW, Rickey DW, Drangova M, Miller DJM, Fenster A. Computer-controlled positive displacement pump for physiological flow simulation. Med Biol Eng Comput 1991; 29:565-570.

Holdsworth DW, Norley CJD, Frayne R, Steinman DA, Rutt BK. Characterization of common carotid artery blood-flow waveforms in normal human subjects. Physiol Meas 1999; 20:219-240

North American Symptomatic Carotid Endarterectomy Trial Steering Committee. North American Symptomatic Carotid Endarterectomy Trial: methods, patients, characteristics and progress. Stroke 1991; 22:771-720

Poepping TL, Nikolov HN, Rankin RN, Lee M, Holdsworth DW. An in vitro system for Doppler ultrasound flow studies in the stenosed carotid artery bifurcation. Ultrasound Med Biol 2002; 28:495-506

Schoning M, Walter J, Scheel P. Estimation of cerebral blood-flow through color duplex sonography of the carotid and vertebral arteries in healthy-adults. Stroke. 1994; 1: 17-22

Smith RF, Rutt BK, Fox AJ, Rankin RN. Geometric characterization of stenosed human carotid arteries. Acad Rad 1996; 3:898-911

Wong EY, Thorne ML, Nikolov HN, Poepping TL, Holdsworth DW. Doppler ultrasound compatible plastic material for use in rigid flow models. Ultrasound Med Biol 2008; 34:1846-1856